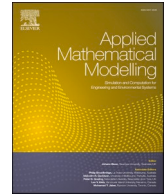




ELSEVIER

Contents lists available at ScienceDirect

## Applied Mathematical Modelling

journal homepage: [www.elsevier.com/locate/apm](http://www.elsevier.com/locate/apm)

## Elastic instabilities of soft laminates with stiffening behavior

Qi Yao<sup>a</sup>, Nitesh Arora<sup>a,b</sup>, Dean Chen<sup>a,c</sup>, Yuhai Xiang<sup>d</sup>, Stephan Rudykh<sup>e,\*</sup><sup>a</sup> Department of Mechanical Engineering, University of Wisconsin, Madison, WI 53706, USA<sup>b</sup> School of Chemical and Biomolecular Engineering, Georgia Institute of Technology, Atlanta, GA 30332, USA<sup>c</sup> Departments of Mechanical and Aerospace Engineering, University of California, Los Angeles, USA<sup>d</sup> Department of Chemical Engineering and Materials Science, University of Minnesota, Minneapolis, MN 55455, USA<sup>e</sup> School of Mathematical and Statistical Sciences, University of Galway, University Road, Galway, Ireland

## ARTICLE INFO

## Keywords:

Nonlinear elasticity  
Hyperelastic materials  
Soft materials  
Layered composites  
Buckling

## ABSTRACT

This paper investigates the elastic instability behavior in soft periodic laminates subjected to finite strains, with a focus on both macroscopic and microscopic instabilities. Considering the deformation-induced phase stiffening, the Gent model with a high bulk-to-shear modulus ratio describes the behavior of incompressible phases. This non-Gaussian statistics-based model captures the non-linear constitutive results from the limited extensibility of polymeric molecular chains. This paper derives an analytical prediction for the onset of macroscopic (or longwave) instability and microscopic instability as functions of material parameters. Moreover, a numerical Bloch-Floquet analysis is imposed on identifying the instability behavior under compression. We consider a wide range of phase combinations and find that the relatively rapid stiffening of the matrix compared to the stiff layer increases the stability of laminates by decreasing the critical stretch ratio. Essentially, properly manipulating the stiffening parameters can produce an absolutely stable region without observed instability. This paper also systematically illustrates the changes in instability and the transition between macro and micro instability in fully Gent laminates, which show higher stability than fully neo-Hookean laminates with larger critical stretch ratios. The critical characteristics of instabilities, such as critical stretch ratios and critical wavenumbers, can be controlled by the choice of stiffening parameters and other material properties, enlarging the tuning of soft laminates for desired buckling patterns in practical applications.

## 1. Introduction

Elastic instability can trigger structural transformations in soft microstructured materials [1–3]. This phenomenon has been applied to designing materials with switchable functionalities and properties [4–7], including negative group velocity [8,9], tunable bandgaps [10–13], energy-absorbing properties [14], and negative Poisson's ratio or auxetic behavior [15–20].

The framework of the linearized small-amplitude motions superimposed on finite deformations (“small-on-large”) is frequently employed to predict the onset of instability [21]. The loss of ellipticity condition can predict the onset of macroscopic (or longwave) instability [22–24]. The effective elastic modulus tensor required by the analysis can be calculated via micromechanics [25,26], numerical simulations [23,25,27–32], or phenomenological models [33–42].

\* Corresponding author at: School of Mathematical and Statistical Sciences, University of Galway, University Road, Galway, Ireland  
E-mail address: [rudykh@wisc.edu](mailto:rudykh@wisc.edu) (S. Rudykh).

<https://doi.org/10.1016/j.apm.2024.03.011>

Received 10 November 2023; Received in revised form 10 March 2024; Accepted 15 March 2024

Available online 20 March 2024

0307-904X/© 2024 The Author(s).

Published by Elsevier Inc.

This is an open access article under the CC BY license

(<http://creativecommons.org/licenses/by/4.0/>).

In microstructured materials, *microscopic* instability may develop at finite wavelengths comparable with the characteristic sizes. Triantafyllidis and Maker [43] studied the microscopic instability in laminates by applying the Bloch-Floquet analysis. Note that the longwave limit in the microscopic instability analysis is equivalent to the loss of ellipticity condition [44]. Slesarenko and Rudykh [45] analyzed the transition between macroscopic and microscopic instabilities in three-dimensional fiber-reinforced composites (FCs) with hyperelastic phases. Galich et al. [46] examined the influence of in-plane fiber arrangement on instability behavior and shear wave propagation along the fiber orientation. Li et al. [47] conducted an experimental investigation on 3D printed specimens, observing the transition between the microscopic buckling pattern and macroscopic mode. Recently, Arora et al. [48] evaluated the influence of constitutive properties and fiber periodicity on buckling direction in FCs with a combination of simulation and experimental measures. Bertoldi and Lopez-Pamies [49] studied the effect of interphases on instability in 2D fiber-reinforced composites. Arora et al. [50] studied the influence of inhomogeneous interphases on buckling in the analogous layered composites. Li et al. [51] reported the experimental observations of twinning microstructure development in the post-buckling regime in soft laminate. Chen et al. [52] examined the instability of soft composites with varying in-plane distributions of the stiff phase; Chen et al. [53] further studied the development of the patterns in the post-buckled domain.

Previous studies of the instability phenomenon in soft composites mostly considered a relatively simple neo-Hookean model to describe the constitutive behavior of the phases [51,53,54]. This weakly non-linear hyperelastic model may not accurately capture the behavior of soft materials [55–66]. Therefore, in this work, we consider a so-called non-Gaussian model for the composite phases and analyze the influence of the strong nonlinearity manifesting in the stiffening effects on the instability of soft laminates. We employ the Gent model [67] to capture the stiffening effects of the phases under finite deformation.

The paper is structured as follows. Section 2 introduces the theoretical background for wave propagation and prediction of instability [21]. Section 3 starts by defining the problem and proposes an effective homogenized strain energy-density function (SEDF) for laminates with Gent phases. Then, we provide a closed-form expression for the critical stretch of macroscopic instability (Section 3.1), which is followed by an analytical prediction for the microscopic instability analysis (Section 3.2). In Section 4.1, we exhibit stress-stretch relationships of the Gent laminates with various material parameters, which is compared with numerical simulations. In the following subsections, we analyzed the influence of the stiffening behavior on the instabilities by examining laminates with (i) single Gent phase and (ii) two Gent phases. Finally, we provide a phase diagram summarizing the dependency of the critical parameters on the phase-locking parameters.

## 2. Theoretical background

The Cartesian position vector of material points in the solid is denoted as vector  $\mathbf{X}$  in the undeformed (or reference) configuration  $\Omega_0$  while that in the deformed configuration  $\Omega$  is  $\mathbf{x}$ . The displacement function for every material point in the body is characterized by the mapping  $\mathbf{x} = \boldsymbol{\chi}(\mathbf{X})$ , with the deformation gradient defined as  $\mathbf{F} = \text{Grad}\boldsymbol{\chi}$ .  $J \equiv \det(\mathbf{F})$  is the ratio between the volumes of an element in the deformed and the undeformed configurations. Consider hyperelastic materials characterized by a scalar-valued energy-density function  $W(\mathbf{F})$  such that

$$\mathbf{P} = \frac{\partial W(\mathbf{F})}{\partial \mathbf{F}}, \tag{1}$$

where  $\mathbf{P}$  is the 1st Piola-Kirchhoff (nominal) stress tensor.

For incompressible materials, Eq. (1) modifies as

$$\mathbf{P} = \frac{\partial W(\mathbf{F})}{\partial \mathbf{F}} - p\mathbf{F}^{-T}, \tag{2}$$

where  $p$  is the Lagrange multiplier.

Correspondingly, the Cauchy stress tensor is

$$\boldsymbol{\sigma} = J^{-1}\mathbf{P}\mathbf{F}^T. \tag{3}$$

The equilibrium equations in the absence of body forces read as

$$\text{div}\boldsymbol{\sigma} = 0, \tag{4}$$

in the deformed configuration. In the reference configuration, the equilibrium equation is

$$\text{Div}\mathbf{P} = 0. \tag{5}$$

Following Ogden [21], we define the incremental deformation gradient as  $\dot{\mathbf{F}} = \partial \dot{\mathbf{u}}/\partial \mathbf{X}$ , where  $\dot{\mathbf{u}}$  is the infinitesimal incremental displacement. The corresponding increment in the first Piola-Kirchhoff stress  $\dot{\mathbf{P}}$  can be expressed through the linearized constitutive relation as

$$\dot{\mathbf{P}} = \mathbb{C}\dot{\mathbf{F}}, \tag{6}$$

where  $\mathbb{C}$  is the tensor of elastic moduli

$$\mathbb{C} = \frac{\partial^2 W}{\partial \mathbf{F} \partial \mathbf{F}}. \tag{7}$$

The components of the push-forward counterpart of the tensor of elastic moduli,  $\mathbb{C}^0$  are

$$C_{i q k p}^0 = J^{-1} F_{p l} F_{q j} C_{i j k l}. \tag{8}$$

The incremental first Piola-Kirchhoff stress  $\dot{\mathbf{P}}$  for incompressible material is

$$\dot{\mathbf{P}} = \mathbb{C} \dot{\mathbf{F}} + p \mathbf{F}^{-T} \dot{\mathbf{F}} \mathbf{F}^{-T} - \dot{p} \mathbf{F}^{-T}, \tag{9}$$

where  $\dot{p}$  is an incremental change in the pressure term related to the incompressibility constraint.

The corresponding incremental updated stress quantity  $\dot{\boldsymbol{\sigma}}$  is derived as

$$\dot{\boldsymbol{\sigma}} = \mathbb{C}^0 \text{grad} \dot{\mathbf{u}} + p (\text{grad} \dot{\mathbf{u}})^T - \dot{p} \mathbf{I}, \tag{10}$$

where  $\text{grad} \dot{\mathbf{u}} = \dot{\mathbf{F}} \mathbf{F}^{-1}$  and  $\mathbf{I}$  is the identity tensor.

The incompressibility condition implies that

$$\nabla \cdot \dot{\mathbf{u}} = 0. \tag{11}$$

The incremental equilibrium equation in the deformed configuration for quasi-static loading is

$$\text{div} \dot{\boldsymbol{\sigma}} = 0. \tag{12}$$

Substituting Eq. (10) into Eq. (12), the equilibrium equation can be written as

$$C_{i q k p}^0 \frac{\partial^2 u_k}{\partial x_q \partial x_p} - \frac{\partial \dot{p}}{\partial x_i} = 0. \tag{13}$$

Seek a solution for Eq. (13) in the form

$$\dot{\mathbf{u}} = \hat{\mathbf{m}} e^{i k x \cdot \hat{\mathbf{n}}}, \quad \dot{p} = q e^{i k x \cdot \hat{\mathbf{n}}}, \tag{14}$$

where  $\hat{\mathbf{m}}$  and  $\hat{\mathbf{n}}$  are unit vectors,  $k$  denotes the wavenumber and  $q$  is a constant. The incompressibility constraint Eq. (11) results in  $\hat{\mathbf{m}} \cdot \hat{\mathbf{n}} = 0$ .

Substituting Eq. (14) into Eq. (13) yields

$$\mathbf{Q} \hat{\mathbf{m}} + i q \hat{\mathbf{n}} = 0, \tag{15}$$

where  $\mathbf{Q}$  is  $Q_{ik} = C_{i q k p}^0 \hat{n}_q \hat{n}_p$  is the acoustic tensor.

The corresponding strong ellipticity condition is

$$Q_{ik} \hat{m}_i \hat{m}_k \equiv C_{i q k p}^0 \hat{n}_q \hat{n}_p \hat{m}_i \hat{m}_k > 0. \tag{16}$$

The condition is commonly used to identify the onset of macroscopic or longwave instabilities [28,31,34,35,38]. The prediction of the microscopic instability in soft composites requires a more demanding analysis, usually employing the Bloch-Floquet technique (see for example, Bertoldi and Boyce [10]).

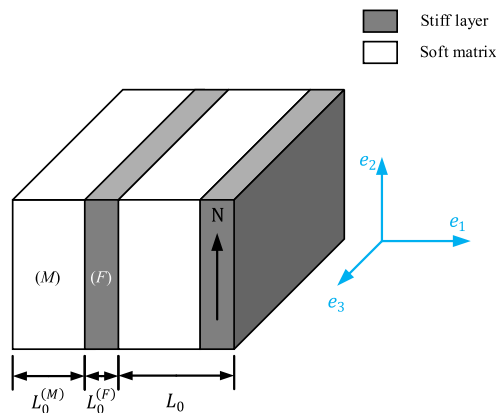


Fig. 1. Schematic of undeformed laminate with periodic distribution of stiff layer aligned along  $e_2$ .

### 3. Analysis and results

Consider a two-phase incompressible laminate with multilayered microstructures, as shown in Fig. 1. The aligned layers are embedded in the soft matrix. Here then, the parameters and fields for phases are denoted by the superscripts  $(\cdot)^{(r)}$  where  $r = M$  represents the soft matrix, and  $r = F$  represents the stiff layer. The phases are homogeneously hyperelastic material with energy-density functions  $W^{(r)}$ . The volume fraction for each phase is  $c^{(r)}$ . The initial direction of the stiff layer is denoted as unit vector  $\mathbf{N}$  in this layer's plane and scalar  $L_0$  is the initial length of the periodic unit cell. The vector  $\mathbf{N}$  is the same as the Cartesian basis vector  $\mathbf{e}_2$ . In the deformed configuration, the direction of the stiff layer and length of the unit cell are  $\mathbf{n}$  and  $L$ , respectively.

The total strain energy-density function (SEDF) of the laminate is

$$\overline{W}(\overline{\mathbf{F}}) = c^{(M)}W^{(M)}(\overline{\mathbf{F}}) + c^{(F)}W^{(F)}(\overline{\mathbf{F}}), \tag{17}$$

where the mean deformation gradient  $\overline{\mathbf{F}} = c^{(M)}\mathbf{F}^{(M)} + c^{(F)}\mathbf{F}^{(F)}$ .

The jump condition for the deformation gradient is

$$[[\mathbf{F}]]\mathbf{N} = 0, \tag{18}$$

where  $[[f]] \equiv (f)^+ - (f)^-$  denotes the difference between the values of any field quantity  $f$  on both sides of an interface.

The deformation gradient in each phase can be obtained by using this condition (see deBotton [68], Rudykh and Boyce [69], for details).

$$\begin{cases} \mathbf{F}^{(M)} = \overline{\mathbf{F}}(\mathbf{I} + \alpha c^{(F)}\mathbf{N} \otimes \mathbf{M}) \\ \mathbf{F}^{(F)} = \overline{\mathbf{F}}(\mathbf{I} - \alpha c^{(M)}\mathbf{N} \otimes \mathbf{M}) \end{cases}, \tag{19}$$

where  $\mathbf{M}$  represents a vector normal to the stiff layer's plane in the reference configuration;  $\mathbf{M} \cdot \mathbf{N} = 0$  and  $\alpha$  is an unknown constant determined through the stress continuity condition

$$[[\mathbf{P}]]\mathbf{M} = 0. \tag{20}$$

Consider laminates with both phases characterized by the Gent strain energy density function (SEDF), namely,

$$W^{(r)}(\mathbf{F}^{(r)}) = -\frac{\mu^{(r)}J_m^{(r)}}{2} \log\left(1 - \frac{I_1^{(r)} - 3}{J_m^{(r)}}\right), \tag{21}$$

where  $I_1^{(r)} = \text{tr}(\mathbf{C}^{(r)}) = \mathbf{F}^{(r)} : \mathbf{F}^{(r)}$  and  $\mathbf{C}^{(r)} = \mathbf{F}^{(r)T}\mathbf{F}^{(r)}$  is the right Cauchy-Green deformation tensor;  $\mu^{(r)}$  and  $J_m^{(r)}$  are the initial shear modulus and the locking parameter of phase  $r$ , respectively. In the limit of  $J_m^{(r)} \rightarrow \infty$ , the Gent model reduces to the neo-Hookean one

$$W^{(r)}(\mathbf{F}^{(r)}) = \frac{\mu^{(r)}}{2} (I_1^{(r)} - 3). \tag{22}$$

The following effective homogenized SEDF for laminates with Gent phases can be constructed [68,70,71]

$$\tilde{W}(\overline{\mathbf{F}}) = \frac{\overline{G}}{2} (I_1 - 3) - \frac{\overline{G} - \tilde{G}}{2} \left( \mathbf{M} \cdot \overline{\mathbf{C}} \cdot \mathbf{M} - \frac{1}{\mathbf{M} \cdot \overline{\mathbf{C}}^{-1} \cdot \mathbf{M}} \right), \tag{23}$$

where  $\overline{\mathbf{C}} = \overline{\mathbf{F}}^T \overline{\mathbf{F}}$ . The effective shear moduli  $\tilde{G}$  and  $\overline{G}$  are

$$\tilde{G} = G^{(M)} \frac{(1 + c^{(F)})G^{(F)} + (1 - c^{(F)})G^{(M)}}{(1 - c^{(F)})G^{(F)} + (1 + c^{(F)})G^{(M)}}, \overline{G} = c^{(M)}G^{(M)} + c^{(F)}G^{(F)}, \tag{24}$$

where  $G^{(r)}$  denotes the tangent shear modulus for phase  $r$ , defined as

$$G^{(r)} = \frac{J_m^{(r)}\mu^{(r)}}{J_m^{(r)} - (I_1^{(r)} - 3)}. \tag{25}$$

In the limit of  $J_m^{(r)} \rightarrow \infty$ , Eq. (23) reduces to the SEDF for laminate with neo-Hookean phases [68,71–73]

$$\tilde{W}(\overline{\mathbf{F}}) = \frac{\overline{\mu}}{2} (I_1 - 3) - \frac{\overline{\mu} - \tilde{\mu}}{2} \left( \mathbf{M} \cdot \overline{\mathbf{C}} \cdot \mathbf{M} - \frac{1}{\mathbf{M} \cdot \overline{\mathbf{C}}^{-1} \cdot \mathbf{M}} \right), \tag{26}$$

where

$$\tilde{\mu} = \mu^{(M)} \frac{(1 + c^{(F)})\mu^{(F)} + (1 - c^{(F)})\mu^{(M)}}{(1 - c^{(F)})\mu^{(F)} + (1 + c^{(F)})\mu^{(M)}}, \overline{\mu} = c^{(M)}\mu^{(M)} + c^{(F)}\mu^{(F)}. \tag{27}$$

For the effective SEDF (23), the macroscopic first Piola-Kirchhoff stress  $\overline{\mathbf{P}}$  read as

$$\bar{\mathbf{P}} = \bar{G}\bar{\mathbf{F}} - \rho\bar{\mathbf{F}}^{-T} - (\bar{G} - \tilde{G})\bar{\mathbf{F}}\mathbf{M} \otimes \mathbf{M} + \frac{\bar{G} - \tilde{G}}{(\bar{\mathbf{F}}^{-T}\mathbf{M} \cdot \bar{\mathbf{F}}^{-T}\mathbf{M})^2}\bar{\mathbf{F}}^{-T}\mathbf{M} \otimes \bar{\mathbf{F}}^{-1}\bar{\mathbf{F}}^{-T}\mathbf{M}. \tag{28}$$

With  $J_m^{(r)} \rightarrow \infty$ , the expression reduces to

$$\bar{\mathbf{P}} = \bar{\mu}\bar{\mathbf{F}} - \rho\bar{\mathbf{F}}^{-T} - (\bar{\mu} - \tilde{\mu})\bar{\mathbf{F}}\mathbf{M} \otimes \mathbf{M} + \frac{\bar{\mu} - \tilde{\mu}}{(\bar{\mathbf{F}}^{-T}\mathbf{M} \cdot \bar{\mathbf{F}}^{-T}\mathbf{M})^2}\bar{\mathbf{F}}^{-T}\mathbf{M} \otimes \bar{\mathbf{F}}^{-1}\bar{\mathbf{F}}^{-T}\mathbf{M}, \tag{29}$$

for the neo-Hookean laminates.

Next, we consider the longwave or macroscopic instabilities in the laminates with the phase stiffening behavior (Section 3.1). This is followed by the microscopic instability analysis in the Gent layered materials (Section 3.2).

### 3.1. Macroscopic instability

In this subsection, we applied the effective homogenized SEDF for Gent laminates (23) in deriving the closed-form critical stretch of macroscopic instability. Consider first the macroscopic deformation of the uniaxial compression with the deformation gradient defined as

$$\bar{\mathbf{F}} = \lambda^{-1/2}\mathbf{e}_1 \otimes \mathbf{e}_1 + \lambda\mathbf{e}_2 \otimes \mathbf{e}_2 + \lambda^{-1/2}\mathbf{e}_3 \otimes \mathbf{e}_3, \tag{30}$$

where  $\lambda$  is the stretch ratio along the stiff layer direction  $\mathbf{e}_2$ . In this paper, the deformation is applied along the vector  $\mathbf{N}$ .

For the uniaxial compression (30), it can be shown that the onset of macroscopic instability in the laminates with Gent phases (23) occurs when the stretch ratio exceeds the critical value given by

$$\lambda^{cr} = \left(1 - \frac{\tilde{G}}{\bar{G}}\right)^{1/3}. \tag{31}$$

In the limit of  $J_m^{(r)} \rightarrow \infty$ , the expression for critical stretch ratio reduces to that corresponding to the neo-Hookean laminates [70]

$$\lambda^{cr} = \left(1 - \frac{\tilde{\mu}}{\bar{\mu}}\right)^{1/3}. \tag{32}$$

Next, we consider the in-plane compression (or pure shear). The corresponding macroscopic deformation gradient is

$$\bar{\mathbf{F}} = \lambda^{-1}\mathbf{e}_1 \otimes \mathbf{e}_1 + \lambda\mathbf{e}_2 \otimes \mathbf{e}_2 + \mathbf{e}_3 \otimes \mathbf{e}_3. \tag{33}$$

For the in-plane deformation, the critical stretch ratio corresponding to the onset of longwave instability in the Gent laminates is

$$\lambda^{cr} = \left(1 - \frac{\tilde{G}}{\bar{G}}\right)^{1/4}. \tag{34}$$

For neo-Hookean laminate, Eq. (34) reduces to [43]

$$\lambda^{cr} = \left(1 - \frac{\tilde{\mu}}{\bar{\mu}}\right)^{1/4}. \tag{35}$$

### 3.2. Microscopic instability

To predict the microscopic instability in the defined Gent laminate, we employ the “small-on-large” approach in which small amplitude motions are superimposed on the finitely deformed state [21]. Here the analysis is performed for the laminates undergoing in-plane deformation (or pure shear) with the deformation gradient (33). We seek a solution for Eq. (13) in the following form

$$\mathbf{u}^{(r)}(x_1, x_2) = \mathbf{v}^{(r)}(x_1)\exp(ik_2x_2) \text{ and } \dot{p}^{(r)}(x_1, x_2) = q^{(r)}(x_1)\exp(ik_2x_2), \tag{36}$$

where  $\mathbf{v}^{(r)}(x_1)$  and  $q^{(r)}(x_1)$  are two undetermined functions of  $x_1$  in phase  $r$  that are required to be solved;  $k_2$  is the wavenumber along the  $\mathbf{e}_2$  direction ( $k_2 \geq 0$ ).

Substitution of  $\mathbf{u}^{(r)}$  in Eq. (36) into the incompressibility constraint (11) leads to

$$ik_2v_2^{(r)} + \frac{d(v_1^{(r)})}{dx_1} = 0. \tag{37}$$

Substitution of Eqs. (36), (37), and (10) into Eq. (12) with the nonzero components (see Appendix A) of the elastic modulus  $\mathbb{C}^{0(r)}$ , leads to the system of linear ordinary differential equations

$$\frac{dq^{(r)}}{dx_1} + k_2^2 C_{1212}^{0(r)} v_1^{(r)} + ik_2 \left( C_{1111}^{0(r)} - C_{1122}^{0(r)} - C_{1221}^{0(r)} \right) \frac{dv_2^{(r)}}{dx_1} = 0, \quad C_{2121}^{0(r)} \frac{d^2 v_2^{(r)}}{dx_1^2} + k_2^2 \left( C_{2112}^{0(r)} + C_{2211}^{0(r)} - C_{2222}^{0(r)} \right) v_2^{(r)} - ik_2 q^{(r)} = 0, \tag{38}$$

where  $v_1^{(r)}$ ,  $v_2^{(r)}$  and  $q^{(r)}$  are unknown variables in each phase ( $r = M, F$ ).

The nonzero components of  $\mathbf{V}^{(r)}$  are

$$V_{12}^{(r)} = -ik_2, \quad V_{23}^{(r)} = 1, \quad V_{32}^{(r)} = -k_2^2 \frac{C_{1212}^{0(r)} + C_{2211}^{0(r)} - C_{2222}^{0(r)}}{C_{2121}^{0(r)}}, \quad V_{34}^{(r)} = ik_2 \frac{1}{C_{2121}^{0(r)}}, \quad V_{41}^{(r)} = -k_2^2 C_{1212}^{0(r)}, \quad V_{43}^{(r)} = -ik_2 \left( C_{1111}^{0(r)} - C_{1122}^{0(r)} - C_{1221}^{0(r)} \right). \tag{39}$$

The differential equation system (38) is transferred into

$$\frac{dy^{(r)}}{dx_1} = \mathbf{V}^{(r)} \mathbf{y}^{(r)}, \tag{40}$$

where  $\mathbf{y}^{(r)} = \left[ v_1^{(r)} \quad v_2^{(r)} \quad \frac{dv_2^{(r)}}{dx_1} \quad q^{(r)} \right]^T$ .

The general solution theory of the ordinary differential equation systems (40) is

$$\mathbf{y}^{(r)}(x_1) = \mathbf{W}^{(r)} \mathbf{Z}^{(r)} \mathbf{a}^{(r)}, \tag{41}$$

where  $4 \times 4$  matrix  $\mathbf{W}^{(r)}$  and  $\mathbf{Z}^{(r)}$  are defined as  $\mathbf{Z}^{(r)} = \text{diag}(\exp(x_1 [z_1^{(r)}, z_2^{(r)}, z_3^{(r)}, z_4^{(r)}]))$ ,  $\mathbf{W}^{(r)} = [w_1^{(r)}, w_2^{(r)}, w_3^{(r)}, w_4^{(r)}]$ . Here,  $z_i^{(r)}$  and  $w_i^{(r)}$  ( $i = 1, 2, 3, 4$ ) denote the eigenvalues and corresponding eigenvectors of the matrix  $\mathbf{V}^{(r)}$ ; vector  $\mathbf{a}^{(r)}$  is a vector of unknown constants.

The solution (41) must satisfy

$$\mathbf{y}^{(M)}(x_1 + L) = \mathbf{y}^{(M)}(x_1) \exp[ik_1 L], \tag{42}$$

where  $k_1$  is a real number ( $0 \leq k_1 \leq 2\pi/L$ ).

For the incremental fields, the continuity conditions on the interface are

$$\llbracket \dot{\mathbf{u}} \rrbracket = 0 \text{ and } \llbracket \dot{\boldsymbol{\sigma}} \rrbracket \mathbf{m} = 0. \tag{43}$$

Here,  $\mathbf{m} = \mathbf{F}^{-T} \mathbf{M}$  is normal to the layer-matrix boundary in the deformed configuration.

Substitution of Eq. (36), Eq. (12), and the Floquet relation (42) into continuity condition (43) yields

$$\mathbf{Q}^{(M)} \mathbf{W}^{(M)} \mathbf{Z}^{(M)}(L) \mathbf{a}^{(M)} = \mathbf{Q}^{(F)} \mathbf{W}^{(F)} \mathbf{Z}^{(F)}(L) \mathbf{a}^{(F)}, \tag{44}$$

and

$$\mathbf{Q}^{(F)} \mathbf{W}^{(F)} \mathbf{Z}^{(F)}(L) \mathbf{a}^{(F)} = \mathbf{Q}^{(M)} \mathbf{W}^{(M)} \mathbf{Z}^{(M)}(L) \mathbf{a}^{(M)}, \tag{45}$$

where the nonzero components of the matrix  $\mathbf{Q}^{(r)}$  are

$$Q_{11}^{(r)} = Q_{22}^{(r)} = 1, \quad Q_{32}^{(r)} = ik_2 \left( C_{1122}^{0(r)} - C_{1111}^{0(r)} - p^{(r)} \right), \quad Q_{32}^{(r)} = -1, \quad Q_{41}^{(r)} = ik_2 p^{(r)}, \quad Q_{43}^{(r)} = C_{2121}^{0(r)}, \tag{46}$$

where  $p^{(r)}$  can be determined from boundary conditions. Eliminating  $\mathbf{a}^{(F)}$  in Eqs. (44) and (45) results in the following relation

$$\left( (\mathbf{G}^{(M)})^{-1} \mathbf{G}^{(F)} \mathbf{Z}^{(F)}(L) (\mathbf{G}^{(F)})^{-1} \mathbf{G}^{(M)} \mathbf{Z}^{(M)}(L) - \exp[ik_1 L] \mathbf{I} \right) \mathbf{a}^{(M)} = 0, \tag{47}$$

where  $\mathbf{G}^{(r)} = \mathbf{Q}^{(r)} \mathbf{W}^{(r)}$ .

The condition for the existence of a nontrivial solution is

$$\det[\mathbf{K} - \exp[ik_1 L] \mathbf{I}] = 0, \tag{48}$$

where

$$\mathbf{K} = (\mathbf{G}^{(M)})^{-1} \mathbf{G}^{(F)} \mathbf{Z}^{(F)}(L) (\mathbf{G}^{(F)})^{-1} \mathbf{G}^{(M)} \mathbf{Z}^{(M)}(L), \tag{49}$$

where  $\det \mathbf{K} = 1$  (since  $\sum_{i=1}^4 z_i^{(r)} = 0$  for all phases). Here the matrix is the  $\mathbf{K}$  characteristic matrix of the differential equation system. The matrix  $\mathbf{K}$  is the function of  $\lambda$  and  $k_2$  when constitutive relationships and geometry of laminate are defined. To detect the onset of instability, we must check if any eigenvalue of the matrix  $\mathbf{K}$  has a magnitude equal to 1 for some positive value of  $k_2$ . This is expressed as  $\|\text{eig}(\mathbf{K})_i\| = 1$  ( $i = 1, 2, 3, 4$ ). The result of the analytical solution is independently verified by the finite element simulations (see Appendix B).

4. Examples

In this section, we examine the effective behavior of Gent laminate and the onset of instability. The results calculated from the analysis in Section 3 are compared with those from numerical simulations.

4.1. Effective behavior of the Gent laminates

Here, we illustrate the effective stress-stretch relationships of the laminates with various combinations of material parameters. For pure shear deformation (30), the effective component of the Cauchy stress tensor is

$$\bar{\sigma} = \bar{\sigma}_{22} - \bar{\sigma}_{11} = (\lambda^2 - \lambda^{-2})\bar{G}. \tag{50}$$

The traction-free boundary condition in  $e_1$  yields the expression of the effective stress component  $\bar{P} = \bar{P}_{22}$

$$\bar{P} = \bar{G}(\lambda - \lambda^{-3}). \tag{51}$$

The dependence of the stress on the stretch ratio can be expressed explicitly, namely,

$$\bar{P} = \left[ \frac{c^{(M)} J_m^{(M)} \mu^{(M)}}{J_m^{(M)} - (\lambda^2 + \lambda^{-2} - 2)} + \frac{c^{(F)} J_m^{(F)} \mu^{(F)}}{J_m^{(F)} - (\lambda^2 + \lambda^{-2} - 2)} \right] (\lambda - \lambda^{-3}). \tag{52}$$

For neo-Hookean laminates, Eq. (51) reduces to  $\bar{P} = \bar{\mu}(\lambda - \lambda^{-3})$ .

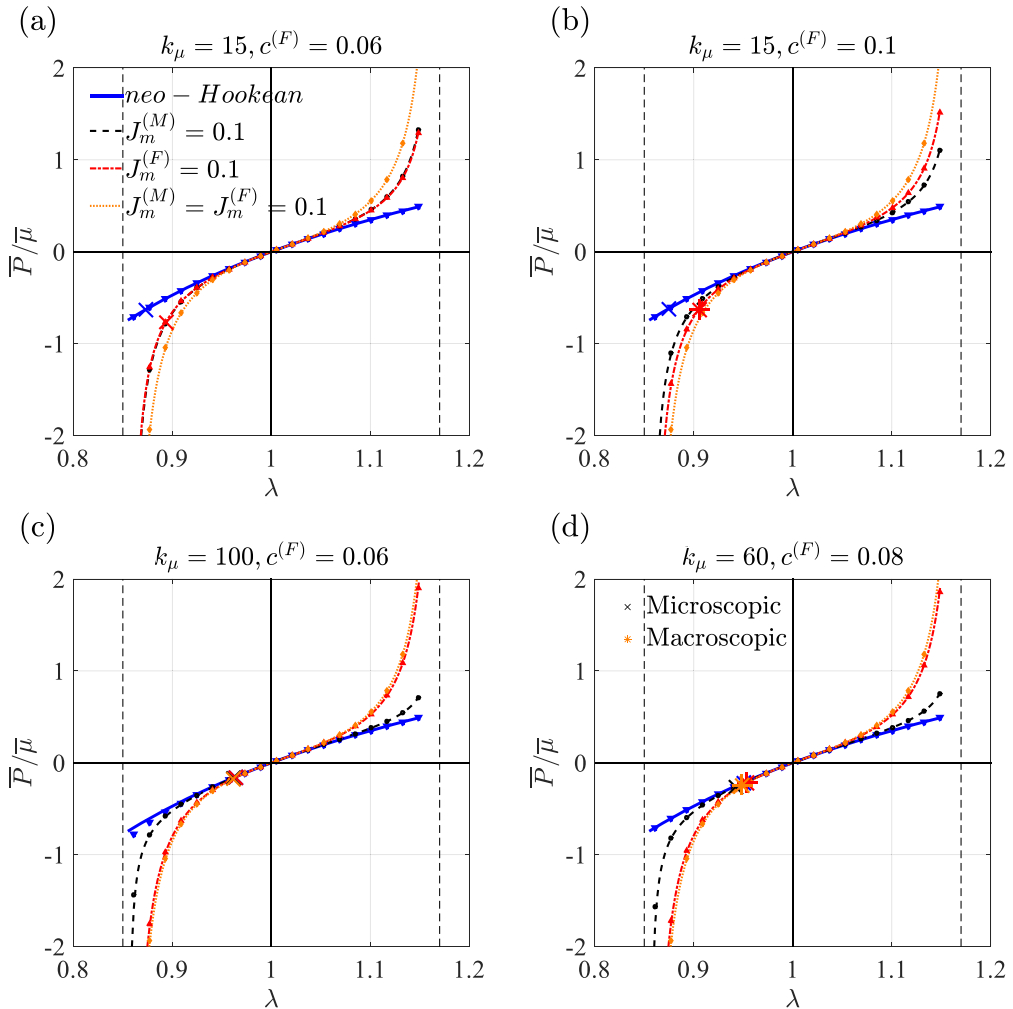


Fig. 2. Normalized stress vs. stretch ratio for the Gent laminates with  $k_\mu = \mu^{(F)}/\mu^{(M)} = 15$  and  $c^{(F)} = 0.06$  (a),  $k_\mu = 15$  and  $c^{(F)} = 0.1$  (b),  $k_\mu = 100$ ,  $c^{(F)} = 0.06$  (c), and  $k_\mu = 60$  and  $c^{(F)} = 0.08$  (d).

Fig. 2 shows the normalized stress  $\bar{P}/\bar{\mu}$  computed by Eq. (52) for the laminates in four combinations: (i) all-neo-Hookean phases (solid blue curves), (ii) Gent matrix ( $J_m^{(M)} = 0.1$ ) and neo-Hookean stiff layers (black dashed curves), and (iii) neo-Hookean matrix and Gent stiff layers ( $J_m^{(F)} = 0.1$ ) (red dash-dot curves), and (iv) all-Gent phases ( $J_m^{(M)} = J_m^{(F)} = 0.1$ ) (orange dotted curves). The results are shown for the composites with initial shear modulus contrast  $k_\mu = 15$  and volume fractions of the stiff layer  $c^{(F)} = 0.06$  (a),  $k_\mu = 15$  and  $c^{(F)} = 0.1$  (b),  $k_\mu = 100$ ,  $c^{(F)} = 0.06$  (c), and  $k_\mu = 60$  and  $c^{(F)} = 0.08$  (d). The analytical expression (48) for the stress-stretch relations (continuous curves) is plotted along with the corresponding FE numerical results (denoted by the discrete scatters of the same color). The vertical dashed lines are locking limits for Gent material with  $J_m = 0.1$ ;  $\lambda_{lock} = 1.17$  for tension and  $\lambda_{lock} = 0.85$  for compression. The onset of instability points is marked by a cross and asterisk for microscopic and longwave instability, respectively. The results show an excellent agreement between the analytical and numerical results.

The results illustrate that the laminates with either all-Gent phases or Gent-neo-Hookean ones experience a significant increase in normalized stress as the stretch ratio approaches the locking limit. As expected, the all-Gent laminates display the most rapid stiffening responses (see the orange-dotted curves and diamond dots with  $J_m = 0.1$  in Fig. 2. In Fig. 2 (a), the stresses in laminates with either Gent matrix ( $J_m^{(M)} = 0.1$ ) and neo-Hookean stiff layer, or Gent stiff layer ( $J_m^{(F)} = 0.1$ ) and the neo-Hookean matrix have similar magnitudes. The increase in stress magnitude due to matrix stiffening is on the approximate level as the stiff layer stiffening with  $c^{(F)} = 0.06$  and  $k_\mu = 15$ . Then, the stress  $\bar{P}$  in laminate Gent matrix and neo-Hookean stiff layer is

$$\bar{P} = \left[ c^{(M)} \frac{J_m^{(M)}}{J_m^{(M)} - (\lambda^2 + \lambda^{-2} - 2)} + c^{(F)} k_\mu \right] \mu^{(M)} (\lambda - \lambda^{-3}), \tag{53}$$

while the stress  $\bar{P}$  in the composite with Gent stiff layer and neo-Hookean matrix is

$$\bar{P} = \left[ c^{(M)} + c^{(F)} k_\mu \frac{J_m^{(F)}}{J_m^{(F)} - (\lambda^2 + \lambda^{-2} - 2)} \right] \mu^{(M)} (\lambda - \lambda^{-3}). \tag{54}$$

With  $k_\mu \cdot c^{(F)} \approx c^{(M)}$ , the stress values in Eqs. (53) and (54) are of similar values since  $J_m^{(M)} = J_m^{(F)}$  and constant volume fraction of the stiff layer in Fig. 2 (a). However, when the volume fraction of the stiff layer is increased to  $c^{(F)} = 0.1$  (see Fig. 2 (b)), the laminate with Gent stiff layer shows a higher stress level than the one with Gent matrix (the  $\bar{P}$  in Eq. (53) is significant that in Eq. (54))

Neo-Hookean laminates with  $k_\mu = 100$  and  $c^{(F)} = 0.06$  (c) and  $k_\mu = 60$  and  $c^{(F)} = 0.08$  (d) experience macroscopic instability, while those with a lower shear modulus contrast,  $k_\mu = 15$  (see Fig. 2 (a) and (b)) buckle in the microscopic mode. The laminates with Gent matrix and neo-Hookean stiff layer in Fig. 2 (a) and (b) do not undergo instability regardless of the deformation level applied; such composites are referred to as absolutely stable. However, for high values of initial shear modulus contrast, such as  $k_\mu = 100$  (c) and  $k_\mu = 60$  (d), the laminates with Gent matrix and neo-Hookean stiff layer experience instability when the corresponding critical stretch is reached. Similarly, the all-Gent laminates with  $k_\mu = 15$  are also stable, while those in Fig. 2 (c) and (d) experience instability. Interestingly, the all-Gent laminates are more stable than their neo-Hookean counterparts, as evidenced by their smaller critical stretch ratios when buckling in microscopic mode (see Fig. 2 (d)). The Gent stiff layer and neo-Hookean matrix laminates experience instability for all the combinations of initial shear modulus contrast and volume fraction of the stiff layer. Their critical stretches are larger than that of their neo-Hookean counterparts. In particular, the laminate with Gent stiff layer buckles in microscopic mode at  $c^{(F)} = 0.06$

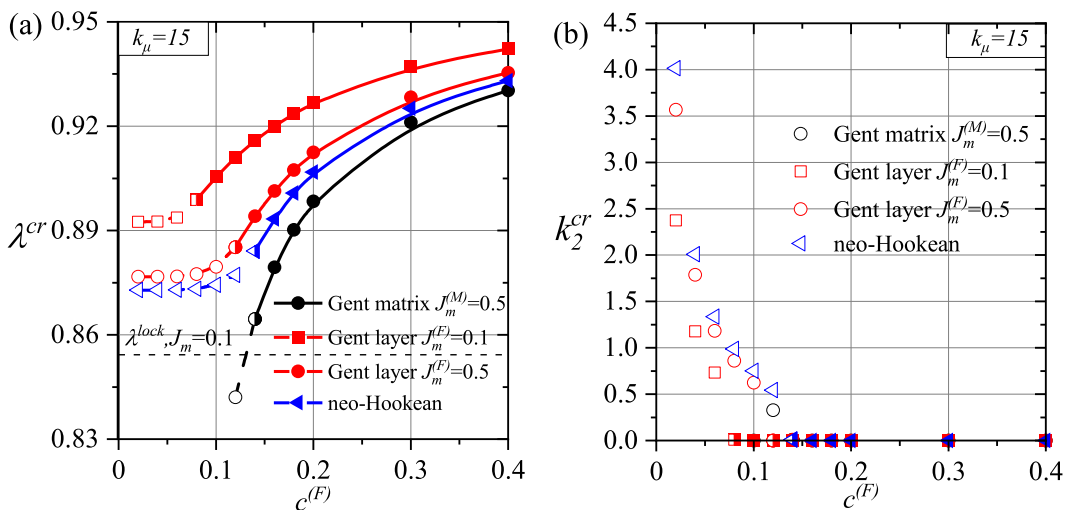


Fig. 3. Critical stretch ratio (a) and normalized critical wavenumber (b) vs. stiff layer volume fraction. The initial shear modulus contrast is  $k_\mu = 15$ . Dashed curves (a) and hollow marks (b) represent the microscopic instabilities; solid curves (a) and filled marks (b) correspond to the longwave instability; half-filled marks show the transition point of instability modes.

(a) while it buckles in longwave mode at  $c^{(F)} = 0.1$  (b). In summary, the stiffening of phases has the potential for tuning the instability behavior, including inducing an absolutely stable state and controlling the appearance of buckling. We discuss the elastic instability in the laminates and the mechanism of tuning it with phase stiffening in detail in the following sections.

#### 4.2. Instabilities in neo-Hookean-Gent laminates

Here, we examine the stability of the “neo-Hookean-Gent” laminates with a phase described by the Gent model, and the other one characterized by the neo-Hookean. The (i) critical stretch  $\lambda^{cr}$  and (ii) normalized critical wavenumber  $k_2^{cr}$  are shown as the functions of stiff layer volume fraction  $c^{(F)}$  with initial shear modulus contrast  $k_\mu = 15$  in Fig. 3 (a) and (b), respectively. Here, three combinations of phases are considered: (i) all-neo-Hookean laminates (blue curve and blue triangles in (a) and (b)); (ii) Gent stiff layer with  $J_m^{(F)} = 0.1, 0.5$  and a neo-Hookean matrix (red curves in (a), red squares and red circles in (b)); (iii) neo-Hookean stiff layer and Gent matrix with  $J_m^{(M)} = 0.5$  (black curve in (a) and black circles in (b)). Here and thereafter, dashed curves and hollow marks denote microscopic instability, while the solid curves correspond to the longwave (or macroscopic) instability; the half-filled marks denote the transition point between the instability modes. A horizontal dashed line represents the locking limits for  $J_m = 0.1$  with  $\lambda_{lock} = 0.8543$ .

For all combinations of phases, the critical stretch ratio increases with the rising stiff layer volume fraction while the normalized critical wavenumber shows a decreasing trend (the critical wavelength increases). The transition point between macro-instability and micro-instability appears on a certain volume fraction of the stiff layer  $c_{cr}^{(F)}$ : when the volume fraction of the stiff layer is larger than this value ( $c^{(F)} > c_{cr}^{(F)}$ ), the laminate buckles in the macroscopic mode. For the laminates with phases (such as laminate with Gent matrix and neo-Hookean stiff layer), the phase stiffening shows a complicated effect on the instability behavior. To discuss the mechanism of tuning instability behavior with phases stiffening, we define the effective shear modulus contrast of stiff layer and matrix as

$$\hat{k}_\mu = \frac{G^{(F)}}{G^{(M)}}. \tag{55}$$

In laminates with Gent phases, the effective shear modulus contrast  $\hat{k}_\mu$  is a function of deformation level  $\lambda$ . Defining the stiffening parameter of both phases as  $g^{(r)} = J_m^{(r)} / (J_m^{(r)} - (I_1^{(r)} - 3))$ , the Eq. (55) is transferred into

$$\hat{k}_\mu = \frac{g^{(F)}}{g^{(M)}} k_\mu. \tag{56}$$

Laminates comprising Gent stiff layer ( $J_m^{(F)} = 0.1, 0.5$ ) and neo-Hookean matrix buckles at larger compressive stretches and exhibits longer critical wavelengths compared to all-neo-Hookean ones. Additionally, the laminates with lower locking parameters of stiff layer buckle earlier (see red curves for  $J_m^{(F)} = 0.1$  and  $J_m^{(F)} = 0.5$  in Fig. 3 (a)). The stiffening of the stiff layer increases the effective shear modulus contrast ( $\hat{k}_\mu > k_\mu$  as  $g^{(F)}$  in Eq. (56) increase) with deformation. Therefore, laminates with Gent stiff layer and neo-Hookean matrix exhibit critical stretches that are larger than all-neo-Hookean ones with  $\hat{k}_\mu = k_\mu$ . Furthermore, the faster stiffening in stiff layers with smaller locking parameters (such as  $J_m^{(F)} = 0.1$  over  $J_m^{(F)} = 0.5$ ) further destabilizes the laminate and induces buckling at lower strain levels. This destabilization mechanism shifts the transition point of instability mode in laminates with Gent stiff layer and neo-Hookean matrix to a smaller volume fraction ( $c_{cr}^{(F)} \approx 0.08$  at  $J_m^{(F)} = 0.1$  and  $c_{cr}^{(F)} \approx 0.12$  at  $J_m^{(F)} = 0.5$ ) compared to all-neo-Hookean counterparts ( $c_{cr}^{(F)} \approx 0.136$ ). This tendency agrees with that observed in neo-Hookean fiber-reinforced composites with increasing initial shear modulus [45].

However, laminates with neo-Hookean stiff layer and Gent matrix ( $J_m^{(M)} = 0.5$ ) buckles at critical stretches smaller than the all-neo-Hookean ones. During the compression, the stiffening parameter of soft matrix in (56) increases rapidly, and the effective shear modulus contrast  $\hat{k}_\mu$  decreases. This stabilization effect requires an increased deformation level to trigger the buckling. Thus, laminates with  $J_m^{(M)} = 0.5$  exhibit critical stretch ratios that are lower than the all-neo-Hookean counterparts. In the extreme situation, the rapid matrix stiffening reduces effective shear modulus contrast to 1 ( $\hat{k}_\mu = 1$  or “stable condition”), resulting in the laminate equivalent to a homogeneous neo-Hookean material. The neo-Hookean stiff layers and Gent matrix laminates with  $J_m^{(M)} = 0.1$  and  $k_\mu = 15$  are observed to be absolutely stable for  $c^{(F)} < 0.4$ . The rapid matrix stiffening at  $J_m^{(M)} = 0.1$  is quick enough to prevent instability from emerging even with a large volume fraction of the stiff layer. Thus, no curve is drawn for  $J_m^{(M)} = 0.1$  in Fig. 3. In contrast, both instability modes and a transition point are observed in laminates with  $J_m^{(M)} = 0.5$ . The transition point of instability mode occurs at a higher volume fraction ( $J_m^{(M)} = 0.5, c_{cr}^{(F)} \approx 0.132$ ) than the all-neo-Hookean ones. Moreover, the laminates with volume fraction of stiff layer  $c^{(F)} = 0.11$  experience instability, while those with  $c^{(F)} < 0.11$  are absolutely stable. The appearance of instability highlights the transition of laminate from an absolutely stable state to an unstable one (transition of stability).

The stiff layer stiffening Fig. 3 shows that both the increase of layer locking parameter  $J_m^{(F)}$  (red curves) and soft matrix locking parameter  $J_m^{(M)}$  (black curve) shifts the curves of the critical stretch ratio and points of critical wavenumber closer to the all-neo-Hookean laminates. This is in line with the fact that when locking parameters are sufficiently large (e.g.,  $J_m^{(M)} = J_m^{(F)} = 1000$ ), the Gent model reduces to the neo-Hookean one. In Fig. 3, the all-neo-Hookean laminates (blue curve) serve as a boundary for separating two stiff layer-matrix combinations. Overall, the stiffening of phases enables us to design absolutely stable laminates with particular

initial shear modulus contrast (for instance,  $J_m^{(M)} = 0.5$ ,  $c^{(F)} = 0.1$  and  $k_\mu = 15$ ). It provides the opportunity for us to tune the absolute stable interval of stiff layer volume fraction and critical parameters by changing  $J_m^{(M)}$  (such as adjusting  $J_m^{(M)}$  between 0.1 and 0.5 for laminates with  $k_\mu = 15$ ).

Fig. 4 shows the influence of the initial shear modulus contrast  $k_\mu$  on the instability behavior in three combinations of phases. The volume fraction of the stiff layer is  $c^{(F)} = 0.08$  and the locking parameter of Gent phases is  $J_m = 0.1$ . Different instability modes and transition points are plotted in the same way as Fig. 3, with a dashed line showing the locking limit of  $J_m = 0.1$ . The critical stretch for all combinations of phases increases with initial shear modulus contrast, and three curves converge. For high initial shear modulus contrast (such as  $k_\mu > 90$  in Fig. 4 (a)), the stiffening of phases does not significantly change the effective shear modulus contrast  $\hat{k}_\mu$  before the onset of instability. This results in close critical stretch ratios. The laminates with Gent matrix ( $J_m^{(M)} = 0.1$ ) show critical stretch ratios that are smaller than the others. On the other hand, the laminates with the Gent stiff layer ( $J_m^{(F)} = 0.1$ ) show the earliest buckling due to higher values of effective shear modulus contrast induced by stiff layer stiffening.

Two transition points are observed in laminates with neo-Hookean stiff layer and Gent matrix: one of the instability modes and the other of stability. First, the instability mode switches at a particular threshold value ( $k_{\mu cr}$ ) from microscopic instability ( $k_\mu < k_{\mu cr}$ ) to macroscopic one ( $k_\mu > k_{\mu cr}$ ). This threshold value is represented by the half-filled black square at  $k_\mu \approx 71$ . As initial shear modulus contrast decreases, the critical stretch ratio decreases until it reaches the locking limit, where the instability disappears. The critical wavenumber in Fig. 4 (b) increases as the locking limit is approached. Restricted by the locking limit, the laminate is stable at a small initial shear modulus contrast, such as  $k_\mu = 20$ . In Fig. 4, the transition of stability appears at  $k_\mu \approx 48$ . For  $k_\mu < 48$ , the quick stiffening of the matrix quickly reduces the effective shear modulus contrast and avoids the onset of instability. For the all-neo-Hookean laminates, the only theoretical stable point is at  $k_\mu = 1$  where the instability does not appear regardless of the compression magnitude. The critical stretches of the blue curve in Fig. 4 (a) descend with the decrease of initial shear modulus contrast. What is not in the figure is that the critical stretch of all-neo-Hookean laminate reaches  $\lambda^{cr} = 0.47$  at  $k_\mu = 2$ . The critical wavenumber of all-neo-Hookean laminate in Fig. 4 (b) decreases after reaching the maximum at  $k_\mu \approx 3$ . This value again shows that the higher shear modulus of the stiff layer to the matrix ( $\hat{k}_\mu > 1$ ) is the necessary condition for the onset of instability. Moreover, the decrease in matrix locking parameter  $J_m^{(M)}$  induces the transition point of stability, which is in agreement with the previous discussion.

The laminates with Gent stiff layer and neo-Hookean matrix (red curve in Fig. 4 (a)) exhibit two transition points of instability modes, which makes them different. Two intervals of macroscopic instability appear in  $k_\mu \gtrsim 47$  and  $k_\mu \lesssim 22$ . In the intermediate interval, the wavenumber first increases to a maximum value ( $22 \lesssim k_\mu \lesssim 35$ ) before decreasing ( $35 \lesssim k_\mu \lesssim 47$ ). With the further increase in initial shear modulus contrast, the wavenumber falls to an approximately zero value where the second transition of instability modes and the onset of macroscopic instability occur. For  $k_\mu \lesssim 22$ , imposing large compression is necessary for activating the instability. This high deformation level leads to significant stiffening of the stiff layer and higher effective shear modulus contrast. As illustrated in previous sections, the all-neo-Hookean laminates tend to lose instability in macroscopic mode at high initial shear modulus contrast. We can draw an explanation that this large compression leads to an effective shear modulus contrast  $\hat{k}_\mu$  equivalent to the initial shear modulus contrast  $k_\mu$  required for inducing macroscopic instability in all-neo-Hookean laminates. In this circumstance, the relationship between instability and initial shear modulus contrast is rather complex. The macroscopic instability at  $k_\mu \gtrsim 47$ , on the other hand, is the result of effective shear modulus contrast enlarged by stiff layer stiffening.

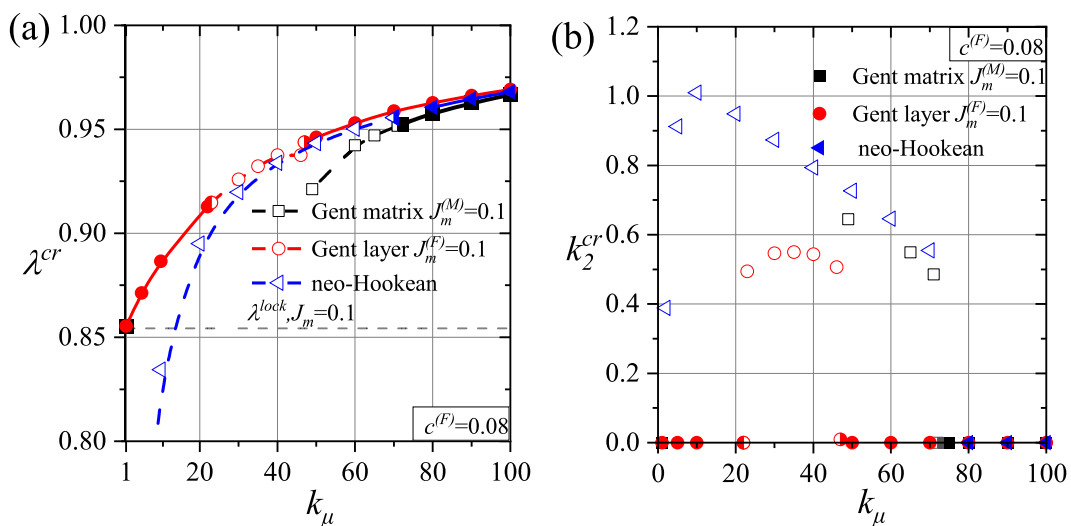


Fig. 4. Critical stretch ratio (a) and normalized critical wavenumber (b) vs. initial shear modulus contrast  $k_\mu$  with volume fraction of stiff layer  $c^{(F)} = 0.08$  and  $J_m = 0.1$ . Dashed curves and hollow marks represent the microscopic instabilities; solid curves and filled marks denote microscopic instabilities. Half-filled marks show the transition point of instability modes.

Fig. 5 (a) and (b) display the critical stretch ratio  $\lambda^{cr}$  and normalized critical wavenumber  $k_2^{cr}$  in three combinations of phases as the function of initial shear modulus contrast  $k_\mu$  with  $J_m = 1$  ( $\lambda_{lock} = 0.618$ ), respectively. The results are similar to those in Fig. 4 but with some notable differences. For example, the laminates with Gent matrix and neo-Hookean stiff layer exhibit a stable interval that is smaller ( $k_\mu < 11$ ) than those with  $J_m^{(M)} = 0.1$ . The slow stiffening at  $J_m^{(M)} = 1$  makes the stable condition ( $\hat{k}_\mu = 1$ ) available when  $k_\mu$  is small. Similarly, two transition points of instability modes are present in the laminates with Gent stiff layer, but the first transition point appears at  $k_\mu \approx 2$ , which is  $k_{\mu cr} \approx 22$  with  $J_m^{(F)} = 0.1$ . The slow stiffening of the stiff layer cannot significantly increase effective shear modulus contrast before the occurrence of instability. Additionally, the critical wavenumber tends to increase and then decrease in the microscopic instability interval as the initial shear modulus contrast increases. Critical wavenumbers higher than those with  $J_m^{(F)} = 0.1$  appear in this interval. It is easy to find that the values and tendency of critical wavenumber are closer to the all-neo-Hookean laminates, which is observed in the laminates with Gent matrix. The overall picture of Fig. 5 shows that the instability behavior of laminates with Gent phases approaches the all-neo-Hookean laminates with increasing locking parameters of Gent phases.

### 4.3. Instabilities in Gent-Gent laminates

This subsection focuses on estimating the ‘‘Gent-Gent’’ laminates with both phases characterized by the Gent model. Fig. 6 (a) and (b) respectively show the critical stretch ratio  $\lambda^{cr}$  and normalized critical wavenumber  $k_2^{cr}$  as functions of stiff layer locking parameter  $J_m^{(F)}$  with matrix locking parameter  $J_m^{(M)}$  fixed at different values ( $J_m^{(M)} = 0.1, 1, 10$ ). The laminates with Gent stiff layer and neo-Hookean matrix (blue curve and blue triangles) are included as a reference. The curves and marks in Fig. 6 are computed with stiff layer volume fraction  $c^{(F)} = 0.06$  and initial shear modulus contrast  $k_\mu = 100$ .

All curves for critical stretch ratio and critical wavelength in Fig. 6 show a decreasing trend as the locking parameter of the stiff layer increases ( $J_m^{(F)}$  increases). The increasing tendency of critical strain and critical wavenumber levels off and enters a platform, as indicated by the horizontal dashed lines. In general, the increasing matrix locking parameter shifts the curves of critical stretch ratio closer to laminates with Gent stiff layer and neo-Hookean matrix. The laminates with high locking parameters of stiff layer (such as  $J_m^{(F)} = 1$ ) lose stability in microscopic mode, while instability transits into the macroscopic mode with  $J_m^{(F)} < J_{m,cr}^{(F)}$  and  $J_{m,cr}^{(F)} \approx 0.04$ . The transition points are marked by half-filled marks in Fig. 6. Here, the changes in the effective shear modulus contrast complicate the activation of the instability. For the values of the matrix locking parameter examined in Fig. 6, the value  $J_{m,cr}^{(F)}$  for the transition point decreases when the matrix locking parameter increases. It is worthwhile to stress that the changes in the transition point  $J_{m,cr}^{(F)}$  is not significant: due to the quick buckling induced by  $k_\mu = 100$ , the stiffening of phases is unable to significantly tune the effective shear modulus contrast before the onset of instability.

Fig. 7 (a) and (b) show the critical stretch ratio  $\lambda^{cr}$  and normalized critical wavenumber  $k_2^{cr}$  as functions of matrix locking parameter  $J_m^{(M)}$  with stiff layer locking parameter  $J_m^{(F)}$  fixed at different values ( $J_m^{(F)} = 0.01, 0.04, 0.1, 1$ ). The laminates with neo-Hookean stiff layer and Gent matrix (blue curve and blue triangles) are included as a reference. The examples in Fig. 7 are computed at the stiff layer volume fraction  $c^{(F)} = 0.06$  and initial shear modulus contrast  $k_\mu = 100$ .

The laminates with all values of the stiff layer locking parameter  $J_m^{(F)}$  tend to lose stability at higher critical stretch ratios as the matrix locking parameter increases. This is induced by the slower stiffening of the matrix and thus higher effective shear modulus

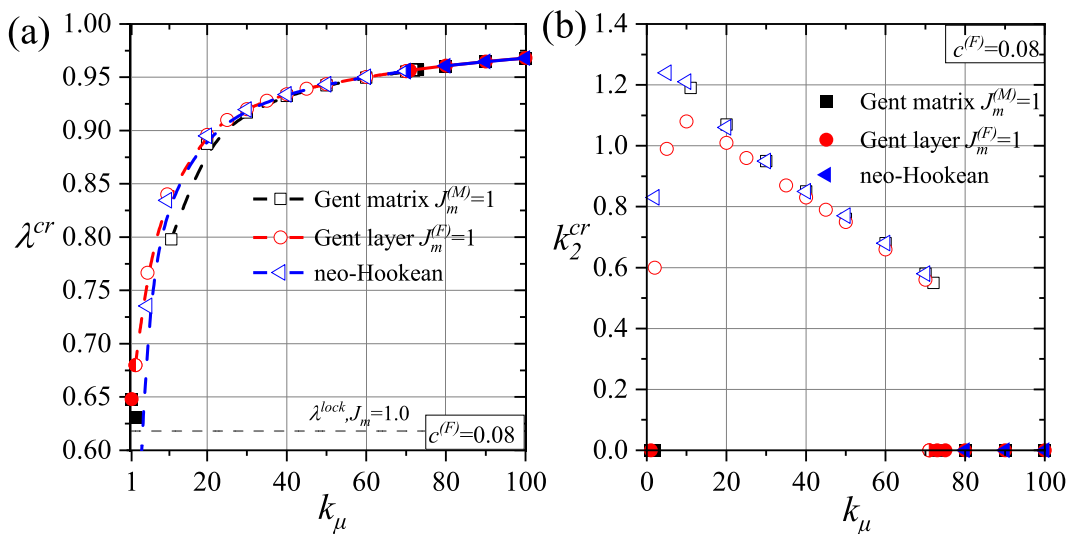


Fig. 5. Critical stretch ratio (a) and normalized critical wavenumber (b) vs. initial shear modulus contrast  $k_\mu$  with volume fraction of stiff layer  $c^{(F)} = 0.08$  and  $J_m = 1$ .

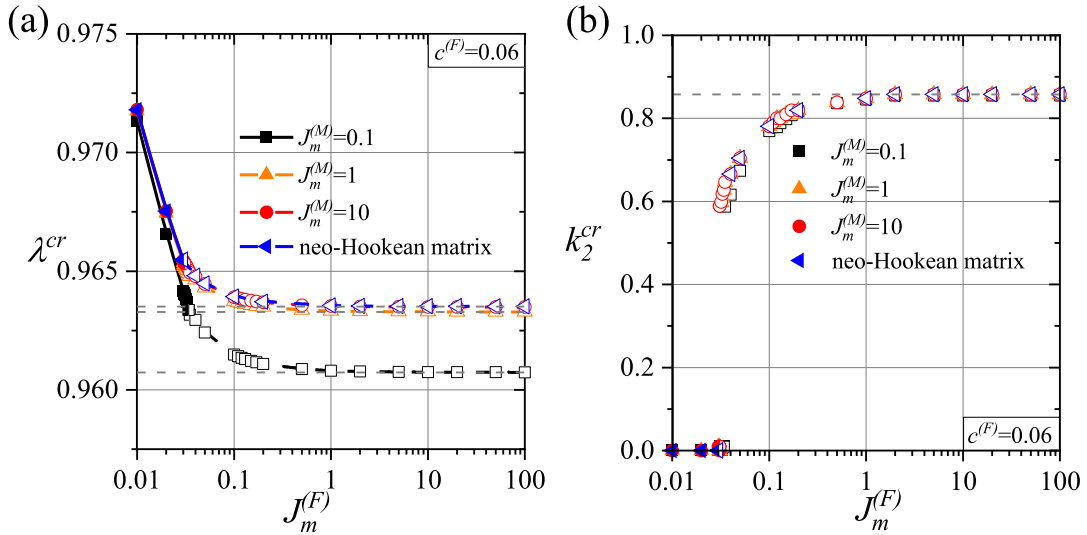


Fig. 6. Critical stretch ratio (a) and normalized critical wavenumber (b) vs. locking parameter  $J_m^{(M)}$  with volume fraction of stiff layer  $c^{(F)} = 0.06$ , initial shear modulus contrast  $k_\mu = 100$ , and  $J_m^{(M)} = 0.1, 1, 10, 1000$ . Different instability modes are marked in the same way as previously done.

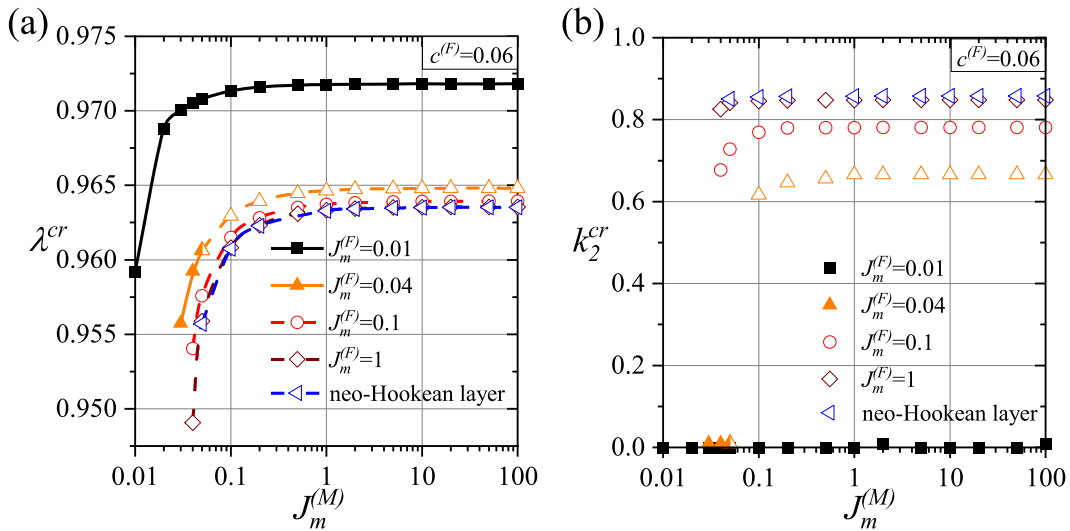


Fig. 7. Critical stretch ratio (a) and normalized critical wavenumber (b) vs. locking parameter  $J_m^{(M)}$  with volume fraction of stiff layer  $c^{(F)} = 0.06$ , initial shear modulus contrast  $k_\mu = 100$ , and  $J_m^{(F)} = 0.01, 0.04, 0.1, 1, 1000$ .

contrast  $\hat{k}_\mu$ , which finally makes it easier for the stiff layer to buckle. All critical stretches enter a section of horizontal curve upon certain thresholds, after which the matrix stiffening imposes negligible effect on effective shear modulus contrast. The locking parameter of the stiff layer significantly varies the instability mode of laminate (Fig. 7 (b)). Moreover, a decrease in the stiff layer locking parameter  $J_m^{(F)}$  leads to earlier buckling in laminates by increasing the effective shear modulus contrast. With the increase of stiff layer locking parameter, the instability behavior transforms from being dominated by longwave instability ( $J_m^{(F)} = 0.01$ ) to a combination of both modes ( $J_m^{(F)} = 0.04$ ) and finally to being dominated by micro-buckling ( $J_m^{(F)} = 0.1, 1, 1000$ ). The laminates with  $J_m^{(F)} = 0.04$  undergo macroscopic instability for  $J_m^{(M)} < 0.05$ . As the locking parameter of the matrix increases, a transition to a micro-instability mode emerges at  $J_m^{(M)} = 0.05$ . The critical wavenumbers for microscopic instability quickly increase and reach a platform as the critical stretch ratio behaves, which is observed at other locking parameters of the stiff layer. On the platform, the variation in locking parameters cannot significantly vary critical parameters. The values of phase locking parameters ( $J_m^{(M)}$  and  $J_m^{(F)}$ ) together determine the buckling mode in a complex way. It is also worth noting that the curve of laminates with neo-Hookean stiff layer ceases

to extend when the matrix locking parameter  $J_m^{(M)}$  decreases to a certain threshold value. When  $J_m^{(M)} < 0.05$ , no instability behavior appears before the laminates are compressed to the locking limit. In Fig. 7 (a), laminates with a neo-Hookean stiff layer serve as a lower bound for all cases.

Finally, we investigate the special cases where the ‘‘Gent-Gent’’ laminates have identical locking parameters ( $J_m^{(M)} = J_m^{(F)} = J_m$ ). Fig. 8 (a) and (b) show the critical stretch  $\lambda^{cr}$  and normalized critical wavenumber  $k_2^{cr}$  as functions of locking parameter  $J_m$  with  $c^{(F)} = 0.06$  and  $0.08$ , and  $k_\mu = 100$ , respectively. The corresponding all-neo-Hookean laminates with the same volume fraction of stiff layer are present as the blue lines and triangles in Fig. 8 (a) and (b), respectively. A black dashed curve highlights the locking limit under compression defined by

$$\lambda_{lock} = \left( \left( J_m + 2 - (J_m^2 + 4J_m)^{1/2} \right) / 2 \right)^{1/2}. \tag{57}$$

In Fig. 8, the laminates with  $c^{(F)} = 0.08$  buckle in macroscopic mode, same as the all-neo-Hookean counterparts. The horizontal sections of the curves indicate that the critical stretch ratio is irrelevant to the variation of the locking parameter. However, the Gent laminates do not buckle when the locking parameter is smaller than a certain threshold due to the locking effect. In contrast, the Gent laminates with  $c^{(F)} = 0.06$  behave differently. From  $J_m = 100$  to  $J_m = 1$ , both the neo-Hookean laminates and Gent laminates undergo microscopic instability at similar critical stretch ratios. As the locking parameter decreases further, the Gent laminates exhibit higher stability with a decreasing critical stretch and eventually lose stability in macroscopic mode, after which critical strain does not significantly increase. On the other hand, microscopic instability appears in the neo-Hookean laminates with  $c^{(F)} = 0.06$ . Therefore, Fig. 8 (a) suggests that the laminates with lower volume fractions of stiff layer are likely to develop microscopic instability, with  $c^{(F)} = 0.06$  on the boundary between macroscopic and longwave instability.

Figs. 6 to 8 exhibit mappings of Gent-Gent laminate instability related to locking parameters as single-variable functions. Fig. 9, on the contrary, displays a complete mapping of instability in Gent-Gent laminates in a dual-variable form, where both critical stretch ratio  $\lambda^{cr}$  and normalized critical wavenumber  $k_2^{cr}$  vary with phase locking parameters. In this mapping, the stiff layer volume fraction is set at  $c^{(F)} = 0.06$ , and the initial shear modulus contrast is  $k_\mu = 100$ . A dash-point curve with half-filled circle marks divides the unstable domain into the macroscopic and microscopic parts. The filled side of the circles is in the macro-instability region. Another curve with half-filled square marks shows the boundary of the stable region. The void side of the square is on the side of the stable region. In the stable region, the instability is not detected before reaching the locking limit.

In general, the laminates with rapid matrix stiffening show small critical stretches. With increasing the locking parameter of the matrix, the width of the stable region decreases. This phenomenon is induced by the quick increases in the effective shear modulus contrast. In the square region bounded by  $J_m^{(F)} \lesssim 0.1$  and  $J_m^{(M)} \lesssim 0.1$ , the changes in instability behavior are more intensified than in other parts where the regular variations can be easily identified. This situation can be attributed to the complex interactions between the quick stiffening of phases. The overall tendency in the unstable region is the gradual decrease in the critical stretch ratio  $\lambda^{cr}$  with an increasing locking parameter of the stiff layer and rapid stiffening of the matrix. In Fig. 9 (a), the increase of stability in laminates with decreasing critical stretch ratios is more significant along the  $J_m^{(F)}$  axis. This increase is especially profound around the boundary of the stable region. Furthermore, the critical wavenumber trends to increase for  $0.03 < J_m^{(F)} < 0.1$ . The variation of critical wavenumber is significant around the transition boundary of instability modes and is much milder when the locking parameters (both for stiff layer and matrix) get larger, such as the region bounded by  $0.1 \lesssim J_m^{(F)} \lesssim 100$  and  $0.1 \lesssim J_m^{(M)} \lesssim 100$ . The transition boundary of instability modes

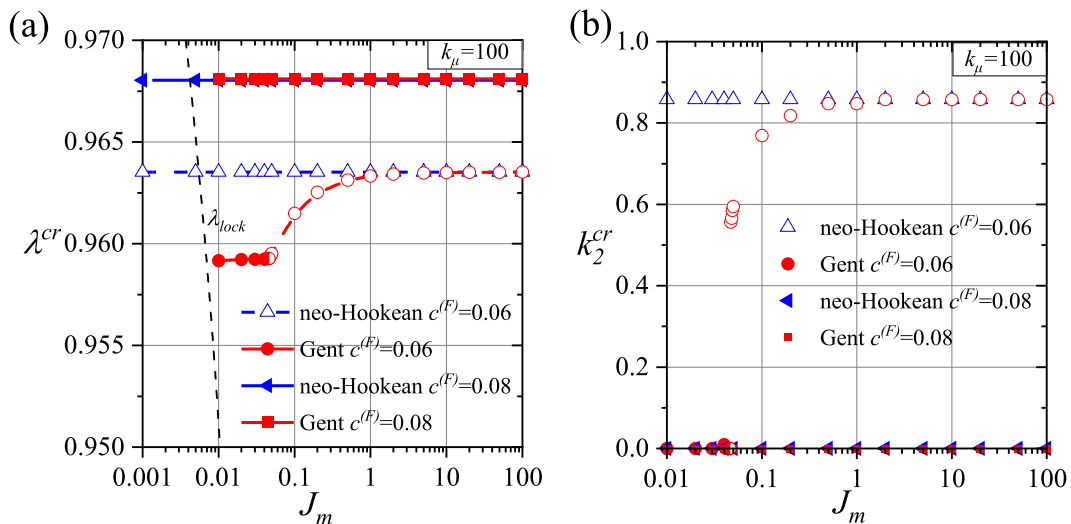
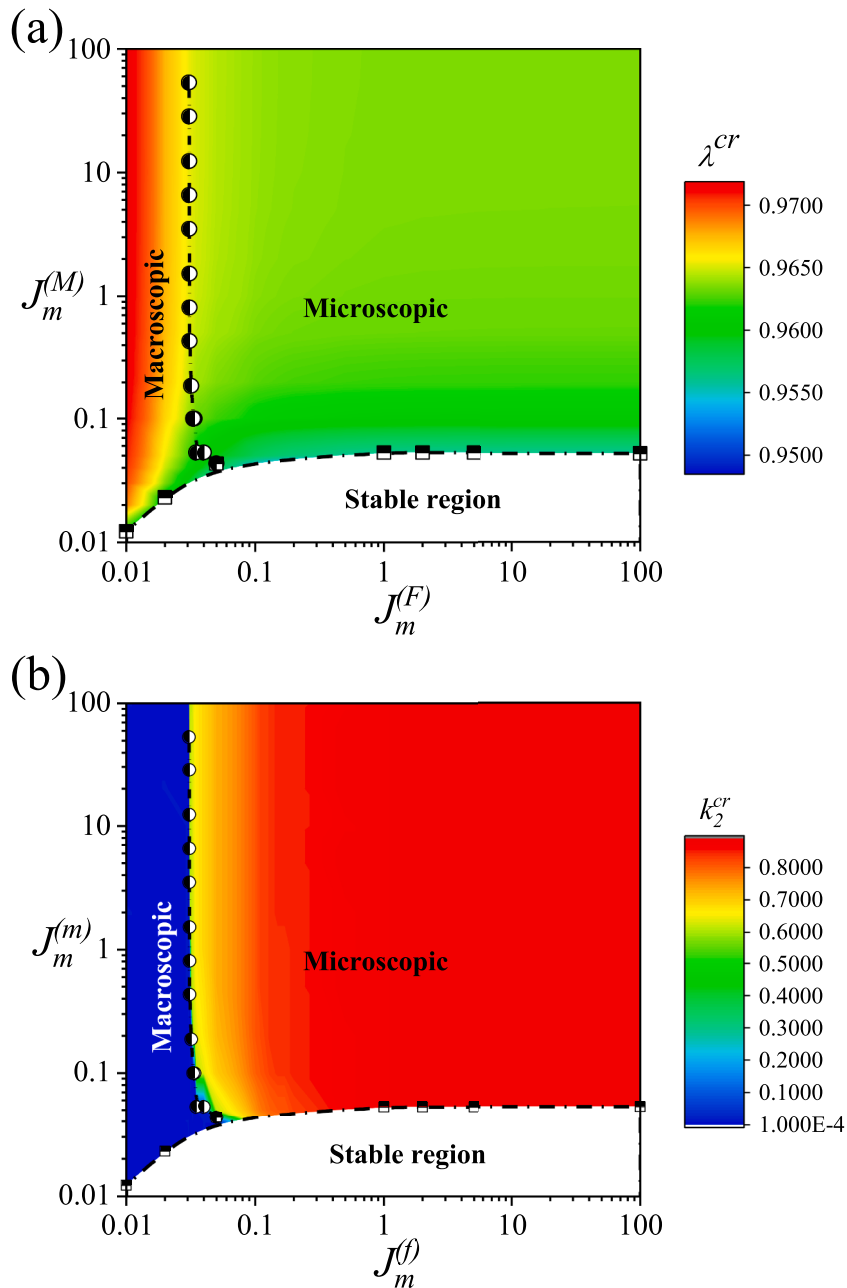


Fig. 8. Critical stretch ratio (a) and normalized critical wavenumber (b) vs. identical locking parameter  $J_m^{(M)} = J_m^{(F)} = J_m$  with volume fraction of stiff layer  $c^{(F)} = 0.06, 0.08$ , and  $k_\mu = 100$ .



**Fig. 9.** Critical stretch ratio (a) and normalized critical wavenumber (b) versus stiff layer locking parameter and matrix locking parameter. The volume fraction of the stiff layer  $c^{(F)} = 0.06$ , and initial shear modulus contrast  $k_\mu = 100$  are considered.

draws a region of macroscopic instability for  $J_m^{(F)} < 0.06$ . This boundary is straight for  $J_m^{(M)} > 0.1$ . Other parts of it with small matrix locking parameters bend toward the increasing side of the stiff layer locking parameter. The laminate tends to lose stability in macroscopic mode or be stable for the smaller locking parameters, such as  $0.01 \lesssim J_m^{(F)} \lesssim 0.05$  and  $0.01 \lesssim J_m^{(M)} \lesssim 0.05$ .

**5. Conclusions**

We studied the elastic instability phenomenon in hyperelastic layered materials with the phases exhibiting the stiffening behavior. In particular, we employed the Gent model to describe the constituent behavior. For the Gent laminates, we derived a closed-form expression for the critical stretch corresponding to the onset of *macroscopic* (or longwave) instability. The expression for the critical stretch reduces to the classical one given for the neo-Hookean laminates (when the Gent model locking parameter becomes large

enough). Moreover, we derived an analytical prediction for the *microscopic* instability in the Gent laminates. We then compared the theoretical results (for the macro- and microscopic instabilities) with our numerical simulations, showing an excellent agreement between those.

Next, we analyzed the influence of the locking parameter on the instabilities in the layered materials. We studied the following combinations of phases: (i) Gent stiff layer and neo-Hookean matrix, (ii) neo-Hookean stiff layer and Gent matrix, and (iii) all-Gent phases. In laminate (i), a decrease in the locking parameter of the stiff layer results in increased critical stretch ratios over all-neo-Hookean counterparts. When the locking parameter of the stiff layer decreases, the volume fraction of the stiff layer, at which instability transits from the macro- to micro-mode, decreases. For laminate (ii), stiffening of the soft matrix stabilizes the composite by reducing the effective shear modulus contrast and, thus, the critical stretch ratios. The matrix stiffening can result in a range of parameters, for which buckling cannot be achieved regardless of the deformation level. We regard these ranges as “absolute stable regions.” In laminates (i) and (ii), the critical wavelength decreases as the effective shear modulus ratio is reduced. The laminate (iii) displays similar critical stretch ratios and wavenumbers as its all-neo-Hookean counterparts when it undergoes longwave buckling. But when the microscopic instability develops, the all-Gent laminates show higher stability than their neo-Hookean counterparts by buckling at smaller critical stretches.

The reported results can further assist in the exploration of soft microstructured composites. The considered instability phenomenon can manifest buckling-activated pattern switches and result in tunable functionalities. These potential functionalities include manipulating electrical and magnetic properties [74–76] and tailoring elastic wave propagation [7,8,11,12,77].

We note that our study focuses on buckling in an idealized laminate model with perfect geometry and homogeneous rate-independent phases. There are different techniques that can be employed to address the uncertainties in constituent behavior [78–81] or geometrical imperfections [82–84]. We note that the frequently observed residual stress is not considered in this study [24]. The influence of residual stress can lead to unforeseen instability behaviors. Additionally, the influence of swelling can be examined [85]. Furthermore, the rate dependency of soft materials may be used for controlling the buckling behavior and patterns [86,87] via loading path and rate. In parallel, the viscoelasticity of the soft materials can be tuned, for example, by adjusting light intensity and other parameters during photo-polymerization [86,88]. We note that the study can be extended to include the effects of the biased fields, such as electric [54,75,89–91], magnetic [76,92–94], thermal loading [95,96]; such external stimuli can induce novel dynamic behavior of the composites. Finally, we note that in the post-buckled regime, the composites may develop into diverse patterns [51, 53]. In this extremely non-linear regime, the stiffening effect may play a significant role in the post-buckling pattern evolution.

**Declaration of competing interest**

The authors declare that they have no known competing financial interests or personal relationships that could have appeared to influence the work reported in this paper.

**Data availability**

Data will be made available on request.

**Acknowledgements**

SR thanks the support of the European Research Council (ERC) through Grant No 852281-MAGIC.

**Appendix A. Components of elastic modulus  $\mathbb{C}^0$  under in-plane tension**

In particular, the components of elastic modulus  $\mathbb{C}^{0(r)}$  for incompressible Gent materials in phase  $r$  are

$$C_{i_1qk p}^{0(r)} = \frac{1}{\det \mathbf{F}^{(r)}} \left( \frac{2\mu^{(r)} J_m^{(r)}}{(J_m^{(r)} - I_1 + 3)^2} B_{qi}^{(r)} B_{pk}^{(r)} + \frac{\mu^{(r)} J_m^{(r)}}{J_m^{(r)} - I_1 + 3} B_{pq}^{(r)} \delta_{ik} \right). \tag{A1}$$

Under the macroscopic deformation gradient specified in Eq. (33), the  $\mathbf{B}^{(r)}$  is

$$\mathbf{B}^{(r)} = \lambda^{-2} \mathbf{e}_1 \otimes \mathbf{e}_1 + \lambda^2 \mathbf{e}_2 \otimes \mathbf{e}_2 + \mathbf{e}_3 \otimes \mathbf{e}_3, \tag{A2}$$

which results in many zero components in  $\mathbb{C}^{0(r)}$ .

**Appendix B. Finite element simulations**

The unit cell in simulations is shown in Fig. A1. The dimensions of the unit cell are  $W = a, H = 0.1a$ , noting that  $H$  is one of the tenths of  $W$  to improve computational efficiency and avoid redundant eigenvalues as done by Slesarenko and Rudykh [45]. The materials of the stiff layer and matrix are defined by the Gent strain-energy function that is integrated into the COMSOL as

$$W^{(r)}(\mathbf{F}^{(r)}) = -\frac{\mu^{(r)}}{2} \log \left( 1 - \frac{I_1^{(r)} - 2}{J_m^{(r)}} \right) + \frac{1}{2} \kappa^{(r)} (J^{(r)} - 1)^2, \quad (\text{A3})$$

where  $\kappa$  is the bulk modulus. To impose a nearly incompressible behavior of the phases, the bulk-to-shear modulus ratio ( $\kappa^{(r)}/\mu^{(r)}$ ) is 1000, which ensures the volume is constant during the simulation. In simulations, two steps are applied consequently to identify the onset point of instability and instability modes that are either macroscopic or microscopic: the first step is quasi-static loading, in which the unit cell is axially compressed along  $\mathbf{e}_2$  under the periodic boundary conditions; the second step is eigenvalue evaluation imposed under the Floquet-Bloch periodicity condition. The Bloch-Floquet periodicity condition expands the incremental displacement  $\mathbf{u}$  of a single unit cell in the deformed configuration into the whole domain:

$$\mathbf{u}(\mathbf{X} + \mathbf{R}) = \mathbf{u}(\mathbf{X}) e^{i\mathbf{K} \cdot \mathbf{R}}, \quad (\text{A4})$$

where  $\mathbf{K} = K_1 \mathbf{e}_1 + K_2 \mathbf{e}_2$  is the Bloch wave vector in the undeformed configuration and  $\mathbf{R} = R_1 W \mathbf{e}_1 + R_2 H \mathbf{e}_2$  is an arbitrary vector with integer coordinates  $R_1, R_2$ . Due to the periodicity in  $\mathbf{e}_1$  and infinite length in  $\mathbf{e}_2$ , the Bloch wave vector  $\mathbf{K}$  under the periodicity condition of laminate is  $\mathbf{K} = (2\pi, K_2)$ . For the Bloch wave vector  $\mathbf{k}$  in the deformed configuration  $\Omega$ ,  $\mathbf{k} = \mathbf{F}^{-T} \mathbf{K}$ .

The specific boundary conditions for both steps are

$$\text{Step1. } \begin{cases} u_{1,DC} = u_{1,AB} + u_{1,B} \\ u_{2,DC} = u_{2,AB} \end{cases}, \begin{cases} u_{1,AD} = u_{1,BC} \\ u_{2,AD} = u_{2,BC} - \varepsilon H \end{cases}, \begin{cases} u_{1,A} = 0 \\ u_{2,A} = 0 \end{cases}, \text{ Step2. } \begin{cases} u_{1,DC} = u_{1,AB} \\ u_{2,DC} = u_{2,AB} \end{cases}, \begin{cases} u_{1,AD} = u_{1,BC} e^{2\pi i k_2 H} \\ u_{2,AD} = u_{2,BC} e^{2\pi i k_2 H} \end{cases}. \quad (\text{A5})$$

Since the buckling only develops along the compression direction, which is the stiff layer orientation  $\mathbf{N}$  in the simulation, only  $k_2$  is scanned; the range of  $k_2$  is from 0 to 5 at every particular deformation level until the instability is identified. Then in the step around the instability point, including all macroscopic instability points and microscopic instability points, is refined to achieve higher accuracy in the critical stretch ratio ( $\lambda^c$ ) and critical wavenumber ( $K_2^c$ ) with only necessary information on computation is here. After accumulating enough cases, some representative computational results are shown in the paper sections.

## References

- [1] D.M. Kochmann, K. Bertoldi, Exploiting microstructural instabilities in solids and structures: from metamaterials to structural transitions, *Appl. Mech. Rev.* 69 (2017) 050801, <https://doi.org/10.1115/1.4037966>.
- [2] J. Li, N. Arora, S. Rudykh, Elastic instabilities, microstructure transformations, and pattern formations in soft materials, *Curr. Opin. Solid State Mater. Sci.* 25 (2021) 100898, <https://doi.org/10.1016/j.cossms.2021.100898>.
- [3] T. Mullin, S. Deschanel, K. Bertoldi, M.C. Boyce, Pattern transformation triggered by deformation, *Phys. Rev. Lett.* 99 (2007) 084301, <https://doi.org/10.1103/PhysRevLett.99.084301>.
- [4] K. Bertoldi, M.C. Boyce, S. Deschanel, S.M. Prange, T. Mullin, Mechanics of deformation-triggered pattern transformations and superelastic behavior in periodic elastomeric structures, *J. Mech. Phys. Solids* 56 (2008) 2642–2668, <https://doi.org/10.1016/j.jmps.2008.03.006>.
- [5] D. Krishnan, H.T. Johnson, Optical properties of two-dimensional polymer photonic crystals after deformation-induced pattern transformations, *J. Mech. Phys. Solids* 57 (2009) 1500–1513, <https://doi.org/10.1016/j.jmps.2009.05.012>.
- [6] A.O. Krushynska, D. Torrent, A.M. Aragón, R. Ardito, O.R. Bilal, B. Bonello, F. Bosia, Y. Chen, J. Christensen, A. Colombi, S.A. Cummer, B. Djafari-Rouhani, F. Fraternali, P.I. Galich, P.D. Garcia, J.-P. Groby, S. Guenneau, M.R. Haberman, M.I. Hussein, S. Janbaz, N. Jiménez, A. Khelif, V. Laude, M.J. Mirzaali, P. Packo, A. Palermo, Y. Pennec, R. Picó, M.R. López, S. Rudykh, M. Serra-Garcia, C.M. Sotomayor Torres, T.A. Starkey, V. Tournat, O.B. Wright, Emerging topics in nanophononics and elastic, acoustic, and mechanical metamaterials: an overview, *Nanophotonics* 12 (2023) 659–686, <https://doi.org/10.1515/nanoph-2022-0671>.
- [7] J. Li, V. Slesarenko, S. Rudykh, Microscopic instabilities and elastic wave propagation in finitely deformed laminates with compressible hyperelastic phases, *Eur. J. Mech. A Solids* 73 (2019) 126–136, <https://doi.org/10.1016/j.euromechsol.2018.07.004>.
- [8] N. Arora, Q. Yao, S. Rudykh, Deformation activated negative group velocity state in soft laminates, *Extrem. Mech. Lett.* (2022) 51, <https://doi.org/10.1016/j.eml.2021.101592>.
- [9] V. Slesarenko, P.I. Galich, J. Li, N.X. Fang, S. Rudykh, Foreshadowing elastic instabilities by negative group velocity in soft composites, *Appl. Phys. Lett.* 113 (2018) 031901, <https://doi.org/10.1063/1.5042077>.
- [10] K. Bertoldi, M.C. Boyce, Wave propagation and instabilities in monolithic and periodically structured elastomeric materials undergoing large deformations, *Phys. Rev. B Condens. Matter Phys.* (2008) 78, <https://doi.org/10.1103/PhysRevB.78.184107>.
- [11] G.Y. Li, Y. Zheng, Y. Cao, X.Q. Feng, W. Zhang, Controlling elastic wave propagation in a soft bilayer system: via wrinkling-induced stress patterns, *Soft Matter* 12 (2016) 4204–4213, <https://doi.org/10.1039/c6sm00265j>.
- [12] J. Li, V. Slesarenko, P.I. Galich, S. Rudykh, Oblique shear wave propagation in finitely deformed layered composites, *Mech. Res. Commun.* 87 (2018) 21–28, <https://doi.org/10.1016/j.mechrescom.2017.12.002>.
- [13] P.I. Galich, A. Sharipova, S. Slesarenko, The emergence of sequential buckling in reconfigurable hexagonal networks embedded into soft matrix, *Materials* 14 (2021) 1–13, <https://doi.org/10.3390/ma14082038> (Basel).
- [14] S. Shan, S.H. Kang, J.R. Rane, P. Wang, L. Fang, F. Candido, J.A. Lewis, K. Bertoldi, Multistable architected materials for trapping elastic strain energy, *Adv. Mater.* 27 (2015) 4296–4301, <https://doi.org/10.1002/adma.201501708>.
- [15] S. Babae, J. Shim, J.C. Weaver, E.R. Chen, N. Patel, K. Bertoldi, 3D soft metamaterials with negative poisson's ratio, *Adv. Mater.* 25 (2013) 5044–5049, <https://doi.org/10.1002/adma.201301986>.
- [16] K. Bertoldi, P.M. Reis, S. Willshaw, T. Mullin, Negative poisson's ratio behavior induced by an elastic instability, *Adv. Mater.* 22 (2010) 361–366, <https://doi.org/10.1002/adma.200901956>.
- [17] B. Florijn, C. Coulais, M. Van Hecke, Programmable mechanical metamaterials, *Phys. Rev. Lett.* 113 (2014) 175503, <https://doi.org/10.1103/PhysRevLett.113.175503>.
- [18] B. Florijn, C. Coulais, M. Van Hecke, Programmable mechanical metamaterials: the role of geometry, *Soft Matter* 12 (2016) 8736–8743, <https://doi.org/10.1039/c6sm01271j>.
- [19] J. Li, V. Slesarenko, S. Rudykh, Auxetic multiphase soft composite material design through instabilities with application for acoustic metamaterials, *Soft Matter* 14 (2018) 6171–6180, <https://doi.org/10.1039/c8sm00874d>.

- [20] J. Li, S. Rudykh, Tunable microstructure transformations and auxetic behavior in 3D-printed multiphase composites: The role of inclusion distribution, *Compos. B Eng.* 172 (2019) 352–362, <https://doi.org/10.1016/j.compositesb.2019.05.012>.
- [21] R.W. Ogden, *Non-Linear Elastic Deformations*, Dover Publications, New York, 1997.
- [22] M. El Hamdaoui, J. Merodio, R.W. Ogden, Deformation induced loss of ellipticity in an anisotropic circular cylindrical tube, *J. Eng. Math.* 109 (2018) 31–45, <https://doi.org/10.1007/s10665-017-9904-z>.
- [23] A. Melnikov, R.W. Ogden, L. Dorfmann, J. Merodio, Bifurcation analysis of elastic residually-stressed circular cylindrical tubes, *Int. J. Solids Struct.* 226–227 (2021) 111062, <https://doi.org/10.1016/j.ijsolstr.2021.111062>.
- [24] J. Merodio, R.W. Ogden, Extension, inflation and torsion of a residually stressed circular cylindrical tube, *Contin. Mech. Thermodyn.* 28 (2016) 157–174, <https://doi.org/10.1007/s00161-015-0411-z>.
- [25] F. Greco, P. Lonetti, R. Luciano, P. Nevone Blasi, A. Pranno, Nonlinear effects in fracture induced failure of compressively loaded fiber reinforced composites, *Compos. Struct.* 189 (2018) 688–699, <https://doi.org/10.1016/j.compstruct.2018.01.014>.
- [26] S. Rudykh, G. Debotton, Instabilities of hyperelastic fiber composites: Micromechanical versus numerical analyses, *J. Elast.* 106 (2012) 123–147, <https://doi.org/10.1007/s10659-011-9313-x>.
- [27] J. Aboudi, R. Gilat, Bifurcation buckling and the effect of imperfections on the microbuckling of soft materials with periodic microstructure by the finite strain HFGMC micromechanics, *Int. J. Solids Struct.* 270 (2023) 112227, <https://doi.org/10.1016/j.ijsolstr.2023.112227>.
- [28] D. Bruno, F. Greco, P. Lonetti, P.N. Blasi, G. Sgambitterra, An investigation on microscopic and macroscopic stability phenomena of composite solids with periodic microstructure, *Int. J. Solids Struct.* 47 (2010) 2806–2824, <https://doi.org/10.1016/j.ijsolstr.2010.06.013>.
- [29] U. De Maio, F. Greco, R. Luciano, G. Sgambitterra, A. Pranno, Microstructural design for elastic wave attenuation in 3D printed nacre-like bioinspired metamaterials lightened with hollow platelets, *Mech. Res. Commun.* 128 (2023) 104045, <https://doi.org/10.1016/j.mechrescom.2023.104045>.
- [30] F. Greco, L. Leonetti, U. De Maio, S. Rudykh, A. Pranno, Macro- and micro-instabilities in incompressible bioinspired composite materials with nacre-like microstructure, *Compos. Struct.* (2021) 269, <https://doi.org/10.1016/j.compstruct.2021.114004>.
- [31] F. Greco, R. Luciano, A theoretical and numerical stability analysis for composite micro-structures by using homogenization theory, *Compos. B Eng.* 42 (2011) 382–401, <https://doi.org/10.1016/j.compositesb.2010.12.006>.
- [32] A. Pranno, F. Greco, L. Leonetti, P. Lonetti, R. Luciano, U. De Maio, Band gap tuning through microscopic instabilities of compressively loaded lightened nacre-like composite metamaterials, *Compos. Struct.* 282 (2022) 115032, <https://doi.org/10.1016/j.compstruct.2021.115032>.
- [33] A.E. Ehret, M. Itskov, A polyconvex hyperelastic model for fiber-reinforced materials in application to soft tissues, *J. Mater. Sci.* 42 (2007) 8853–8863, <https://doi.org/10.1007/s10853-007-1812-6>.
- [34] J. Merodio, R.W. Ogden, Material instabilities in fiber-reinforced nonlinearly elastic solids under plane deformation, *Arch. Mech.* 54 (2002) 525–552.
- [35] J. Merodio, R.W. Ogden, Instabilities and loss of ellipticity in fiber-reinforced compressible non-linearly elastic solids under plane deformation, *Int. J. Solids Struct.* 40 (2003) 4707–4727, [https://doi.org/10.1016/S0020-7683\(03\)00309-3](https://doi.org/10.1016/S0020-7683(03)00309-3).
- [36] J. Merodio, R.W. Ogden, Remarks on instabilities and ellipticity for a fiber-reinforced compressible nonlinearly elastic solid under plane deformation, *Q. Appl. Math.* 63 (2005) 325–333, <https://doi.org/10.1090/s0033-569x-05-00954-1>.
- [37] J. Merodio, R.W. Ogden, Tensile instabilities and ellipticity in fiber-reinforced compressible non-linearly elastic solids, *Int. J. Eng. Sci.* 43 (2005) 697–706, <https://doi.org/10.1016/j.iijengsci.2005.01.001>.
- [38] J. Merodio, T.J. Pence, Kink surfaces in a directionally reinforced neo-Hookean material under plane deformation: II. Kink band stability and maximally dissipative band broadening, *J. Elast.* 62 (2001) 145–170, <https://doi.org/10.1023/A:1011693326593>.
- [39] J. Merodio, T.J. Pence, Kink surfaces in a directionally reinforced neo-Hookean material under plane deformation: I. Mechanical equilibrium, *J. Elast.* 62 (2001) 119–144, <https://doi.org/10.1023/A:1011625509754>.
- [40] G.Y. Qiu, T.J. Pence, Loss of ellipticity in plane deformation of a simple directionally reinforced incompressible nonlinearly elastic solid, *J. Elast.* 49 (1997) 31–63, <https://doi.org/10.1023/A:1007441804480>.
- [41] K.Y. Volokh, Loss of ellipticity in elasticity with energy limiters, *Eur. J. Mech. A Solids* 63 (2017) 36–42, <https://doi.org/10.1016/j.euromechsol.2016.10.003>.
- [42] M. El Hamdaoui, J. Merodio, R.W. Ogden, Two-phase piecewise homogeneous plane deformations of a fibre-reinforced neo-Hookean material with application to fibre kinking and splitting, *J. Mech. Phys. Solids* 143 (2020) 104091, <https://doi.org/10.1016/j.jmps.2020.104091>.
- [43] N. Triantafyllidis, B.N. Maker, On the comparison between microscopic and macroscopic instability mechanisms in a class of fiber-reinforced composites, *J. Appl. Mech. Trans. ASME* 52 (1985) 794–800, <https://doi.org/10.1115/1.3169148>.
- [44] G. Geymonat, S. Müller, N. Triantafyllidis, Homogenization of nonlinearly elastic materials, microscopic bifurcation and macroscopic loss of rank-one convexity, *Arch. Ration. Mech. Anal.* 122 (1993) 231–290, <https://doi.org/10.1007/BF00380256>.
- [45] V. Slesarenko, S. Rudykh, Microscopic and macroscopic instabilities in hyperelastic fiber composites, *J. Mech. Phys. Solids* 99 (2017) 471–482, <https://doi.org/10.1016/j.jmps.2016.11.002>.
- [46] P.I. Galich, V. Slesarenko, J. Li, S. Rudykh, Elastic instabilities and shear waves in hyperelastic composites with various periodic fiber arrangements, *Int. J. Eng. Sci.* 130 (2018) 51–61, <https://doi.org/10.1016/j.iijengsci.2018.05.003>.
- [47] J. Li, V. Slesarenko, P.I. Galich, S. Rudykh, Instabilities and pattern formations in 3D-printed deformable fiber composites, *Compos. B Eng.* 148 (2018) 114–122, <https://doi.org/10.1016/j.compositesb.2018.04.049>.
- [48] N. Arora, J. Li, S. Rudykh, Tunable buckling configurations via in-plane periodicity in soft 3D-fiber composites: Simulations and experiments, *Int. J. Solids Struct.* 250 (2022) 111711, <https://doi.org/10.1016/j.ijsolstr.2022.111711>.
- [49] K. Bertoldi, O. Lopez-Pamies, Some remarks on the effect of interphases on the mechanical response and stability of fiber-reinforced elastomers, *J. Appl. Mech. Trans. ASME* 79 (2012) 031023, <https://doi.org/10.1115/1.4006024>.
- [50] N. Arora, A. Batan, J. Li, V. Slesarenko, S. Rudykh, On the influence of inhomogeneous interphase layers on instabilities in hyperelastic composites, *Materials* 12 (2019) 763, <https://doi.org/10.3390/ma12050763> (Basel).
- [51] J. Li, V. Slesarenko, S. Rudykh, Emergence of instability-driven domains in soft stratified materials, *Npj Comput. Mater.* 8 (2022) 1–6, <https://doi.org/10.1038/s41524-022-00783-x>.
- [52] D. Chen, N. Arora, Y. Xiang, J. Li, V. Slesarenko, S. Rudykh, Instability-induced patterns and their post-buckling development in soft particulate composites, *Mech. Mater.* (2022) 175, <https://doi.org/10.1016/j.mechmat.2022.104482>.
- [53] D. Chen, Y. Xiang, N. Arora, Q. Yao, J. Li, S. Rudykh, Post-buckling development in soft particulate composites, *Compos. Struct.* 322 (2023) 117337, <https://doi.org/10.1016/j.compstruct.2023.117337>.
- [54] M. Bahreman, N. Arora, H. Darjani, S. Rudykh, Structural and material electro-mechanical instabilities in microstructured dielectric elastomer plates, *Eur. J. Mech. A Solids* 94 (2022) 104534, <https://doi.org/10.1016/j.euromechsol.2022.104534>.
- [55] M.C. Wang, E. Guth, Statistical theory of networks of non-gaussian flexible chains, *J. Chem. Phys.* 20 (1952) 1144–1157, <https://doi.org/10.1063/1.1700682>.
- [56] Y. Xiang, D. Zhong, S. Rudykh, H. Zhou, S. Qu, W. Yang, A review of physically based and thermodynamically based constitutive models for soft materials, *J. Appl. Mech. Trans. ASME* 87 (2020) 110801, <https://doi.org/10.1115/1.4047776>.
- [57] Y. Xiang, D. Zhong, P. Wang, G. Mao, H. Yu, S. Qu, A general constitutive model of soft elastomers, *J. Mech. Phys. Solids* 117 (2018) 110–122, <https://doi.org/10.1016/j.jmps.2018.04.016>.
- [58] P.I. Galich, S. Rudykh, Influence of stiffening on elastic wave propagation in extremely deformed soft matter: From nearly incompressible to auxetic materials, *Extrem. Mech. Lett.* 4 (2015) 156–161, <https://doi.org/10.1016/j.eml.2015.06.003>.
- [59] Y. Xiang, C. Schilling, N. Arora, A.J. Boydston, S. Rudykh, Mechanical characterization and constitutive modeling of visco-hyperelasticity of photocured polymers, *Addit. Manuf.* 36 (2020) 101511, <https://doi.org/10.1016/j.addma.2020.101511>.
- [60] E.M. Arruda, M.C. Boyce, A three-dimensional constitutive model for the large stretch behavior of rubber elastic materials, *J. Mech. Phys. Solids* 41 (1993) 389–412, [https://doi.org/10.1016/0022-5096\(93\)90013-6](https://doi.org/10.1016/0022-5096(93)90013-6).

- [61] J.D. Davidson, N.C. Goulbourne, A nonaffine network model for elastomers undergoing finite deformations, *J. Mech. Phys. Solids* 61 (2013) 1784–1797, <https://doi.org/10.1016/j.jmps.2013.03.009>.
- [62] S.F. Edwards, T. Vilgis, The effect of entanglements in rubber elasticity, *Polymer* 27 (1986) 483–492, [https://doi.org/10.1016/0032-3861\(86\)90231-4](https://doi.org/10.1016/0032-3861(86)90231-4) (Guildf).
- [63] M. Itskov, A.E. Ehret, R. Dargazany, A full-network rubber elasticity model based on analytical integration, *Math. Mech. Solids* 15 (2010) 655–671, <https://doi.org/10.1177/1081286509106441>.
- [64] H.M. James, E. Guth, Theory of the elastic properties of rubber, *J. Chem. Phys.* 11 (1943) 455–481, <https://doi.org/10.1063/1.1723785>.
- [65] M. Kaliske, G. Heinrich, An extended tube-model for rubber elasticity : Statistical-mechanical theory and finite element implementation, *Rubber Chem. Technol.* 72 (1999) 602–632, <https://doi.org/10.5254/1.3538822>.
- [66] W. Kuhn, F. Grün, Beziehungen zwischen elastischen konstanten und dehnungsdoppelbrechung hochelastischer stoffe, *Kolloid Z.* 101 (1942) 248–271, <https://doi.org/10.1007/BF01793684>.
- [67] A.N. Gent, A new constitutive relation for rubber, *Rubber Chem. Technol.* 69 (1996) 59–61, <https://doi.org/10.5254/1.3538357>.
- [68] G. deBotton, Transversely isotropic sequentially laminated composites in finite elasticity, *J. Mech. Phys. Solids* 53 (2005) 1334–1361, <https://doi.org/10.1016/j.jmps.2005.01.006>.
- [69] S. Rudykh, M.C. Boyce, Analysis of elastoid fish imbricated layered scale-tissue systems and their bio-inspired analogues at finite strains and bending, *IMA, J. Appl. Math.* 79 (2014) 830–847, <https://doi.org/10.1093/imat/hxu005>.
- [70] P.I. Galich, N.X. Fang, M.C. Boyce, S. Rudykh, Elastic wave propagation in finitely deformed layered materials, *J. Mech. Phys. Solids* 98 (2017) 390–410, <https://doi.org/10.1016/j.jmps.2016.10.002>.
- [71] S.A. Spinelli, O. Lopez-Pamies, Some simple explicit results for the elastic dielectric properties and stability of layered composites, *Int. J. Eng. Sci.* 88 (2015) 15–28, <https://doi.org/10.1016/j.ijengsci.2014.01.005>.
- [72] P.I. Galich, V. Slesarenko, S. Rudykh, Shear wave propagation in finitely deformed 3D fiber-reinforced composites, *Int. J. Solids Struct.* 110–111 (2017) 294–304, <https://doi.org/10.1016/j.ijsolstr.2016.12.007>.
- [73] P.I. Galich, S. Rudykh, Shear wave propagation and band gaps in finitely deformed dielectric elastomer laminates: Long wave estimates and exact solution, *J. Appl. Mech. Trans. ASME* 84 (2017) 091002, <https://doi.org/10.1115/1.4037159>.
- [74] A. Goshkoderia, N. Arora, V. Slesarenko, J. Li, V. Chen, A. Juhl, P. Buskohl, S. Rudykh, Tunable permittivity in dielectric elastomer composites under finite strains: Periodicity, randomness, and instabilities, *Int. J. Mech. Sci.* 186 (2020) 105880, <https://doi.org/10.1016/j.ijmecsci.2020.105880>.
- [75] M.R. O'Neill, D. Sessions, N. Arora, V.W. Chen, A. Juhl, G.H. Huff, S. Rudykh, R.F. Shephard, P.R. Buskohl, Dielectric elastomer architectures with strain-tunable permittivity, *Adv. Mater. Technol.* 7 (2022), <https://doi.org/10.1002/admt.202200296>.
- [76] P. Pathak, N. Arora, S. Rudykh, Magnetoelastic instabilities in soft laminates with ferromagnetic hyperelastic phases, *Int. J. Mech. Sci.* 213 (2022) 106862, <https://doi.org/10.1016/j.ijmecsci.2021.106862>.
- [77] N. Arora, Y. Xiang, S. Rudykh, Multiscale analysis of elastic waves in soft materials: From molecular chain networks to fiber composites, *Int. J. Mech. Sci.* 200 (2021) 106433, <https://doi.org/10.1016/j.ijmecsci.2021.106433>.
- [78] P. Hauseux, J.S. Hale, S.P.A. Bordas, Accelerating Monte Carlo estimation with derivatives of high-level finite element models, *Comput. Methods Appl. Mech. Eng.* 318 (2017) 917–936, <https://doi.org/10.1016/j.cma.2017.01.041>.
- [79] P. Hauseux, J.S. Hale, S. Cotin, S.P.A. Bordas, Quantifying the uncertainty in a hyperelastic soft tissue model with stochastic parameters, *Appl. Math. Model.* 62 (2018) 86–102, <https://doi.org/10.1016/j.apm.2018.04.021>.
- [80] H. Rappel, L.A.A. Beex, L. Noels, S.P.A. Bordas, Identifying elastoplastic parameters with Bayes' theorem considering output error, input error and model uncertainty, *Probabilistic Eng. Mech.* 55 (2019) 28–41, <https://doi.org/10.1016/j.proengmech.2018.08.004>.
- [81] M. Zeraatpisheh, S.P.A. Bordas, L.A.A. Beex, Bayesian model uncertainty quantification for hyperelastic soft tissue models, *Data-Centric Eng.* 2 (2021) E9, <https://doi.org/10.1017/dce.2021.9>.
- [82] L.L. Chen, H. Lian, Z. Liu, H.B. Chen, E. Atroshchenko, S.P.A. Bordas, Structural shape optimization of three dimensional acoustic problems with isogeometric boundary element methods, *Comput. Methods Appl. Mech. Eng.* 355 (2019) 926–951, <https://doi.org/10.1016/j.cma.2019.06.012>.
- [83] C. Ding, R.R. Deokar, Y. Ding, G. Li, X. Cui, K.K. Tamma, S.P.A. Bordas, Model order reduction accelerated Monte Carlo stochastic isogeometric method for the analysis of structures with high-dimensional and independent material uncertainties, *Comput. Methods Appl. Mech. Eng.* 349 (2019) 266–284, <https://doi.org/10.1016/j.cma.2019.02.004>.
- [84] P. Yu, S.P.A. Bordas, P. Kerfriden, Adaptive Isogeometric analysis for transient dynamics: Space–time refinement based on hierarchical a-posteriori error estimations, *Comput. Methods Appl. Mech. Eng.* 394 (2022) 114774, <https://doi.org/10.1016/j.cma.2022.114774>.
- [85] H. Topol, M.J. Al-Chalhawi, H. Demirkoparan, J. Merodio, Bifurcation of Fiber-Reinforced Cylindrical Membranes under Inflation, and Swelling, *J. Appl. Comput. Mech.* 9 (2023) 113–128, <https://doi.org/10.22055/jacm.2022.40949.3677>.
- [86] Y. Xiang, D. Chen, N. Arora, Q. Yao, S. Rudykh, Towards understanding the role of viscoelasticity in microstructural buckling in soft particulate composites, *Compos. B Eng.* 263 (2023) 110850, <https://doi.org/10.1016/j.compositesb.2023.110850>.
- [87] V. Slesarenko, S. Rudykh, Harnessing viscoelasticity and instabilities for tuning wavy patterns in soft layered composites, *Soft Matter* 12 (2016) 3677–3682, <https://doi.org/10.1039/c5sm02949j>.
- [88] J. Wu, Z. Zhao, C.M. Hamel, X. Mu, X. Kuang, Z. Guo, H.J. Qi, Evolution of material properties during free radical photopolymerization, *J. Mech. Phys. Solids* 112 (2018) 25–49, <https://doi.org/10.1016/j.jmps.2017.11.018>.
- [89] S. Rudykh, K. Bhattacharya, G. DeBotton, Snap-through actuation of thick-wall electroactive balloons, *Int. J. Non Linear. Mech.* 47 (2012) 206–209, <https://doi.org/10.1016/j.ijnonlinmec.2011.05.006>.
- [90] A. Goshkoderia, S. Rudykh, Electromechanical macroscopic instabilities in soft dielectric elastomer composites with periodic microstructures, *Eur. J. Mech. A Solids* 65 (2017) 243–256, <https://doi.org/10.1016/j.euromechsol.2017.04.008>.
- [91] S. Rudykh, G. deBotton, Stability of anisotropic electroactive polymers with application to layered media, *Z. Angew. Math. Phys.* 62 (2011) 1131–1142, <https://doi.org/10.1007/s00033-011-0136-1>.
- [92] A. Goshkoderia, V. Chen, J. Li, A. Juhl, P. Buskohl, S. Rudykh, Instability-induced pattern formations in soft magnetoactive composites, *Phys. Rev. Lett.* 124 (2020) 158002, <https://doi.org/10.1103/PhysRevLett.124.158002>.
- [93] V.W. Chen, N. Arora, A. Goshkoderia, C.L. Willey, Z. Turgut, P.R. Buskohl, S. Rudykh, A.T. Juhl, Mechanical instability tuning of a magnetorheological elastomer composite laminate, *Compos. B Eng.* 251 (2023) 110472, <https://doi.org/10.1016/j.compositesb.2022.110472>.
- [94] S. Rudykh, K. Bertoldi, Stability of anisotropic magnetorheological elastomers in finite deformations: a micromechanical approach, *J. Mech. Phys. Solids* 61 (2013) 949–967, <https://doi.org/10.1016/j.jmps.2012.12.008>.
- [95] C. Yuan, X. Mu, C.K. Dunn, J. Haidar, T. Wang, H. Jerry Qi, Thermomechanically triggered two-stage pattern switching of 2D lattices for adaptive structures, *Adv. Funct. Mater.* 28 (2018) 1–9, <https://doi.org/10.1002/adfm.201705727>.
- [96] K. Che, M. Rouleau, J. Meaud, Temperature-tunable time-dependent snapping of viscoelastic metastructures with snap-through instabilities, *Extrem. Mech. Lett.* 32 (2019) 100528, <https://doi.org/10.1016/j.eml.2019.100528>.